This is a preprint, the final version is subject to change, of the American Mineralogist (MSA)
Cite as Authors (Year) Title. American Mineralogist, in press.
DOI: https://doi.org/10.2138/am-2018-6473

Revision 2

On the relative timing of listwaenite formation and chromian spinel equilibration in serpentinites

Hisham A. Gahlan[1,2], Mokhles K. Azer[3], Paul D. Asimow[4]

[1]*Department of Geology and Geophysics, King Saud University, Riyadh 11451, Saudi Arabia*

[2]*Geology Department, Assiut University, Assiut 71516, Egypt*

[3]*Geological Sciences Department, National Research Centre, Cairo, Egypt*

[4]*Division of Geological & Planetary Sciences, California Institute of Technology, USA*

Abstract

Ultramafic rocks exposed at the Earth's surface generally record multiple stages of evolution that may include melt extraction, serpentinization, carbonatization, and metamorphism. When quantitative thermometry based on mineral chemistry is applied to such rocks, it is often unclear what stage of their evolution is being observed. Here, in peridotites with extensive replacement of silicate minerals by carbonates (listwaenites), we present a case study that addresses the timing of carbonate formation relative to closure of exchange reactions among relict primary minerals.

Massive and schistose serpentinized peridotites of Neoproterozoic age outcrop at Gabal Sirsir, South Eastern Desert, Egypt (northwestern corner of the Arabian-Nubian Shield, ANS). Petrography, bulk composition, and mineral chemistry are all consistent with a strongly depleted mantle harzburgite protolith for the serpentinites. Bulk compositions are low in Al_2O_3 and CaO and high in Mg# [molar Mg/(Mg+Fe) = 0.89–0.93]. Relict spinel has high Cr# [molar Cr/(Cr+Al)] and low Ti, while relict olivine has high Mg# and NiO contents. Based on compositions of coexisting relict olivine and chromian spinel, the protolith experienced 19 to

21% partial melt extraction. Such high degrees of partial melting indicate a supra-subduction zone environment, possibly a forearc setting.

Along thrust faults and shear zones, serpentinites are highly altered to form talc-carbonate rocks and weathering-resistant listwaenites that can be distinguished petrographically into Types I and II. The listwaenitization process took place through two metasomatic stages, associated first with formation of the oceanic crustal section and near-ridge processes (~750-700 Ma) and subsequently during obduction associated with the collision of East and West Gondwana and escape tectonics (~650-600 Ma). In the first stage, Mg# of chromian spinel in the serpentinites continuously changed due to subsolidus Mg–Fe^{2+} redistribution, while the Mg# of chromian spinel in the Type I listwaenites was frozen due to the absence of coexisting mafic silicates. During the second stage, the Type II listwaenites formed along shear zones accompanied by oxidation of relict chromian spinel to form ferritchromite and Cr-bearing magnetite in both serpentinites and listwaenites. The high Cr# of chromian spinel relicts in both serpentinites and listwaenites preserves primary evidence of protolith melt extraction, but divalent cations are more easily mobilized at low temperature. Hence, relict chromian spinel in listwaenites shows significantly higher Mg# and lower MnO than that in serpentinite, suggesting that nearly complete alteration of ultramafic rocks to form listwaenite took place prior to re-equilibration between chromian spinel and the surrounding mafic minerals in serpentinites. Furthermore, the ferritchromite in the serpentinites has higher Mn content (1.1–2.1 wt%) than that in the listwaenites (0.6-0.9wt%), indicating its formation after carbonatization since carbonate minerals are a favorable sink for Mn.

Keywords: Arabian-Nubian Shield, Neoproterozoic, Serpentinite, Listwaenite

1. Introduction

Listwaenite is a term used for carbonated meta-ultramafic rocks that commonly bear fuchsite-quartz-carbonate mineral paragenesis (e.g, Halls and Zhao, 1995; Gahlan et al., 2015a) and represent the end products of various degrees of carbonatization, potassium alteration, and silicification. Alternate spellings include listvenite and listvanite (Kelemen et al. 2011) and roughly interchangeable names for the same rock type include 'Barramiya rocks' and 'carbonated meta-ultramafics' (e.g. Rittmann 1958; Azer 2013; Gahlan et al. 2015a; Boskabadi et al. 2017; Sofiya et al. 2017). They are often associated with talc-carbonate rocks. During the listwaenitization process, primary ferromagnesian silicate minerals in ultramafic rocks are replaced by carbonate minerals and the released silica forms quartz (Uçurum 2000). Fuchsite, the common name for the green Cr-rich variety of muscovite, is the result of potassium metasomatism. Carbonated meta-ultramafic rocks in the Eastern Desert of Egypt, especially listwaenites, have drawn attention because of their economic potential, including gold mineralization (e.g. Botros 1993; Osman 1995; Botros 2002, 2004; Ramadan 2002; Ramadan et al. 2005; Abd El-Rahman et al. 2012; Azer 2013; Gahlan et al. 2015a; Boskabadi et al. 2017) that has been mined since Pharaonic times (Harraz, 2000; Klemm et al., 2001).

Chromian spinel is a nearly ubiquitous accessory mineral in ultramafic and many mafic rocks. It has been used successfully as a geotectonic and petrogenetic indicator mineral (e.g. Irvine 1965, 1967; Dick and Bullen 1984; Arai 1992, 1994) because its composition is notably sensitive to changes in temperature, pressure, oxygen fugacity, bulk rock and fluid composition (e.g. Irvine 1965, 1967) and because it resists low-temperature alteration processes that may affect every other phase in an ultramafic sample. The sensitivity of spinel Cr# in particular to the degree of partial melting extraction has been widely applied as a geotectonic indicator for upper-mantle derived peridotites (e.g. Dick and Bullen 1984; Arai 1994).

The obduction of ophiolites in the Arabian-Nubian Shield (ANS) was accompanied by several kinds of alteration (e.g. Azer and Stern 2007; Stern et al. 2004; Azer 2013, Boskabadi et al. 2017). A characteristic feature in the ANS ophiolites is the major abundance of carbonate alteration along shear zones in the ultramafic rocks, but the sources and fluxes of the CO_2-rich fluids that drove this carbonate alteration and its timing relative to other events in the evolution of the rocks are unknown.

The current research offers a detailed report on the geological, mineralogical, and geochemical characteristics of the serpentinized peridotites and their alteration products at Gabal (G.) Sirsir, Wadi Hodein district, South Eastern Desert, Egypt. No detailed petrological or geochemical study of this occurrence has been published before. Although the serpentinization and carbonatization processes largely obliterated primary petrological characteristics of the G. Sirsir peridotites, primary relics of mantle olivine and chromian spinel have been used as petrogenetic indicators. We focus on the evidence of alteration and achievement of equilibrium between chromian spinel and coexisting minerals, which provides a good opportunity to constrain the relative timing of the epoch in the evolution of the rocks recorded by the spinel chemistry and of the events leading to carbonatization of the ultramafic rocks to form listwaenite. A similar approach to the listwaenite occurrences in Ethiopia was recently published by Sofiya et al. (2017); we compare our results and conclusions to theirs below.

2. Geological outline

The Arabian-Nubian Shield (ANS) is a juvenile tract of continental crust that forms the northern part of the East African Orogen (e.g. Stern 1994, 2002; Jarrar et al. 2003; Johnson and Woldehaimanot 2003; Meert 2003; Stoeser and Frost 2006). It formed in the Neoproterozoic through multiple stages of accretion and arc development along several suture zones. Ophiolitic

rocks are scattered through most of the ANS. They represent fragments of oceanic lithosphere obducted on the continental margins during collision between East and West Gondwana and closure of the Mozambique Ocean. Such Neoproterozoic ophiolites are common in the central and south Eastern Desert of Egypt (Fig. 1), the north western corner of the ANS. Reconstructing the pseudolithostratigraphic column of the Egyptian ophiolites shows that they represent remnants of oceanic lithosphere that formed in a supra-subduction zone setting during Neoproterozoic time (e.g. Stern et al. 2004; Azer and Stern 2007; Ali et al. 2010; Azer et al. 2013; Khalil et al. 2014; Gahlan et al. 2015b; Obeid et al. 2016).

Complete ophiolite sections are rare (but present) in the Eastern Desert of Egypt. They generally consist of a lower serpentinized ultramafic unit and an upper unit of layered and isotropic gabbros, sheeted dykes, and massive or rarely pillow basalts (e.g. El Sharkawy and El Bayoumi 1979; El Bayoumi 1983; Gahlan et al. 2015b). However, most of the Egyptian ophiolites are variably dismembered, deformed, altered, and metamorphosed due to serpentinization and interaction with a large flux of CO_2-bearing fluids (Stern and Gwinn 1990; Gahlan et al. 2015a; Boskabadi et al. 2017). The alteration is focused along shear zones and faults and led to formation of various types of carbonate-bearing meta-ultramafics.

The G. Sirsir area forms the southern part of the Wadi Hodein district in the South Eastern Desert (SED) of Egypt, ~20 km west-northwest of Shalatin City (Fig. 1). It features outcrops of Neoproterozoic basement rocks including an ophiolite sequence, an island arc association, and late- to post-tectonic granites (Fig. 2). Basement rocks in the area were affected by a regional compressional regime (WSW–ENE) expressed by NW-trending folds and WSW-verging thrust faults, but many earlier phases of structural deformation can be recognized as well (e.g., Abdeen et al. 2008). The G. Sirsir ophiolite fragments are polydeformed allochthonous megashear masses in a tectonic mélange and include serpentinized ultramafics, metagabbros and pillow metabasalts.

The island-arc association is represented by variably deformed metasediments, metavolcanics and a metagabbro-diorite complex. The deformed metagabbro-diorite rocks intrude the ophiolitic mélange matrix and the island arc metavolcaniclastics. The metavolcaniclastics, serpentinites and carbonatized serpentinites (listwaenites) are subsequently intruded by the late- to post-orogenic granites, with notable granite offshoots.

The variably serpentinized and carbonatized ophiolitic ultramafic rocks form the mantle section of the G. Sirsir ophiolite (Fig. 2). They form lenses and sheets striking NW–SE and dipping by ~50º SW, tectonically incorporated in a mélange with metasediments and metavolcaniclastics. Serpentinites are generally massive and homogeneous, dominated by harzburgite with less abundant dunite. Along shear zones and toward the sole thrust, they are transformed into schistose serpentinites, listwaenites and talc-carbonate rocks. Mesoscopic network veins (2–20 cm thick) of magnesite and quartz cross-cut both serpentinites and talc-carbonates. Also, small masses and irregular pockets of magnesite are observed in the sheared carbonatized serpentinite. Talc-carbonate rocks occur as variably sheared blocks, sheets and lenses along the NW and NNW–SSE fault zones.

The talc-carbonate rocks are brownish to greenish grey and can be either massive or highly schistose. On the other hand, listwaenite form rootless reddish cream-colored sheets, ridges, and irregular lenses and masses along shear zones and fault planes (up to 3000 m long and 500 m wide). They express positive geomorphic relief relative to the surrounding rocks due to their resistance to arid-climate weathering. Structural elements in the listwaenite rocks are generally conformable to the main plano-linear fabric of the host country rocks (Fig. 2). Along contacts, the listwaenites show no chilled margins, reaction haloes or xenoliths from the host. The characteristic reddish cream weathered surface and porous texture are the result of supergene oxidative weathering of Fe-bearing carbonates to form iron oxides. Two types of listwaenite have

been identified, Type I and II (Fig. 3). Type I is typical listwaenite. Although Type II might best be called a listwaenite-like rock, we will refer to it herein as Type II listwaenite. Type I is fuchsite-bearing and low in modal quartz; it is found spatially associated with serpentinites in yellowish-green colored NW-SE striking deformed lenses with prominent schistosity (Figs. 3a and b). By contrast, Type II is fuchsite-free with more abundant quartz and is spatially associated with granites in WNW-ENE striking, undeformed, reddish-cream or yellowish masses, locally brecciated and fractured (fractures are filled with carbonate veinlets and fine quartz ribbons) (Figs. 3c and d).

3. Methodology

Mineral identification in polished thin sections was accomplished using a Polarizing Nikon Microscope, environmental scanning electron microscope (ESEM), and electron probe micro-analyzer (EPMA), supplemented by powder X-ray diffraction (XRD) analyses. XRD analyses used a BRUKER D8 advanced X-ray diffractometer in the Central Metallurgical and Development Institute, Cairo, Egypt, with Cu radiation and a secondary monochrometer. Scanning speed was 2θ=1deg/min at constant voltage 40kV and current 40mA. Mineral identification was referenced to both d-spacing and relative intensities of reflections using the American Standard Test Materials (ASTM) cards.

Some polished sections of listwaenite samples were examined with a Philips XL30 environmental scanning electron microscope (ESEM) at the Nuclear Materials Authority in Egypt, operating at 25kV and equipped with energy dispersive analytical X-ray (EDAX) capability. The spectrometer detects elements with atomic number greater than 4 (*e.g.*, B) and a count rate ~ 1000-1500 counts per second.

Mineral chemistry of relict primary (olivine and spinel) and metamorphic minerals were determined with an electron microprobe at the Geology and Metallogeny Laboratory, Orléans, France. Operating conditions were 15kV accelerating voltage, 20nA beam current and 3µm beam diameter. Suitable synthetic and natural silicate and oxide standards were applied for calibration. Carbonate standards were not used for the carbonate mineral analyses; rather these were quality-controlled by computing the weight of CO_2 necessary to stoichiometrically balance the measured FeO+MnO+MgO+CaO. Samples whose total estimated this way did not yield 100±2 wt. % were discarded.

Whole-rock chemical analyses (major oxides and trace elements) of powdered rock samples (12 listwaenites and 8 serpentinites) were carried out at ACME Analytical Laboratories in Vancouver, Canada. The analyzed serpentinite samples were carefully selected to avoid carbonate or quartz veinlets. Samples were analysed by Inductively Coupled Plasma-Mass Spectrometry (ICP-MS) following a lithium metaborate/tetraborate fusion and nitric acid digestion of a 0.2 g sample. The detection limits are between 0.01% and 0.04% for major elements, and between 0.01 and 0.5 ppm for most of the trace elements, except Au (0.5 ppb) and Ni (20 ppm). Analytical precision, as calculated from replicate analyses, is 0.5–1.0 % for major elements and varies from 5% to 20% for trace elements. Loss on ignition (LOI) is determined by weight difference after ignition at 1000ºC.

4. Petrography

4.1. Serpentinites

The massive and sheared serpentinites of G. Sirsir are notably similar in composition, but the later has a schistosity defined by subparallel alignment of serpentine flakes. The massive serpentinite consists mainly of antigorite with lesser amounts of chrysotile, lizardite, magnesite,

talc, chlorite, brucite and magnetite (quantitative mineral identification by XRD). There are trace relics of primary olivine and chromian spinel. Locally, a few serpentinite samples are rich in carbonates (up to 40 vol%). The serpentine minerals replacing olivine exhibit mesh texture (Fig. 4a), while those replacing orthopyroxene exhibit bastite texture (10–15 vol%) (Fig. 4b), suggesting dunite and harzburgite protoliths.

Antigorite forms fibro-lamellar or flame-like crystals and interpenetrating texture. Occasionally, antigorite is intergrown with magnesite (Fig. 4c). The chrysotile long fibers form veinlets cross-cutting the antigorite matrix, indicating protracted serpentinization. Carbonates are stained reddish brown by iron oxides. In general, the carbonates occur as scattered aggregates (Fig. 4d), as cross-cutting cryptocrystalline veinlets and crack-fill, or as replacement of mesh texture. Talc occurs as flakes or fine-grained matrix associated with carbonates. Brucite appears as platy or fibrous crystals intermixed with serpentines and as veinlets.

Chromian spinel morphology appears to be independent of whether the host rock is schistose. It forms subhedral and anhedral crystals in serpentinized dunites and amoeboid or vermicular (Fig. 4e) crystals in serpentinized harzburgites. Rarely, it forms euhedral cubic crystals and cumulate layers. Along grain boundaries and cracks, chromian spinel is partially replaced by an irregular ferritchromite mantle (light-grey colored) and a magnetite rim (grey-white colored) (Fig. 4e). A few altered chromian spinel rims are surrounded by aureoles of faintly pleochroic flakes, from violet to deep violet, of chromian chlorite (the variety commonly called kämmererite). Magnetite forms scattered anhedral to euhedral crystals throughout serpentinites. In addition, magnetite develops as rims around chromian spinel or replacing mesh centers and rims. Disseminated sulfides — including pyrite, pentlandite and rare chalcopyrite — are observed scattered throughout the serpentinites and variably altered. Pyrite occurs as euhedral to subhedral

disseminated crystals or as inclusions in magnetite. Pentlandite occurs as rounded grains, slightly altered to garnierite and magnetite along margins.

4.2. Listwaenites

Petrographically, two types of listwaenite can be identified: Type I (typical listwaenite with fuchsite; Figure 4f) and Type II (listwaenite-like rocks without fuchsite). Although listwaenites form along shear zones, most samples do not show any preferred orientation or schistosity. Type I listwaenite is composed essentially of carbonates (50-60 vol. %), quartz (35-45%) and minor fuchsite, with accessory Fe-Ti oxides, serpentine, chromian spinel and chlorite. The carbonates are mainly magnesite and breunnerite, with minor amounts of calcite and dolomite. Breunnerite clearly formed at the expense of primary carbonates and is sometimes in turn replaced by Fe–Mn oxides. Fuchsite has a dark emerald-green color. It forms flakes as well as fine disseminated crystals and thin bands with a perfect cleavage in one direction (Fig. 4f), sometimes intergrown with chlorite. A few magnesite veinlets are observed cross-cutting the groundmass. The chromian spinel forms subhedral fractured grains with ferritchromite developed along grain boundaries and cracks (Fig. 4g). The ferritchromite zone around primary spinel is consistently thinner in Type I listwaenites (Fig. 4g) than that in serpentinites. Polished thin sections revealed minor disseminated sulphides and scarce native gold.

The Type II listwaenite (fuchsite-free listwaenite-like rocks) has typically slightly more modal quartz (40-45 %) and lower abundance of carbonate minerals (45-60%) than Type I listwaenite. The accessory minerals include Fe-Ti oxides, chromian spinel, muscovite, chlorite, and sulfides. Reflected-light microscopy shows that Type II listwaenites are richer in opaque minerals (~2.0-2.5 % by volume) than Type-I listwaenites (<1.5 %). The opaque minerals include pyrite, chalcopyrite, galena, sphalerite, covellite, goethite, magnetite and gold. The carbonate

minerals are mainly magnesite with less calcite and dolomite. Chromian spinel is mostly anhedral, fractured and highly altered to ferritchromite (Fig. 4h). The alteration of chromian spinel in the Type II listwaenite is more extensive than that in the Type I listwaenite. In general, the petrography of our Type II listwaenite appears similar to all the samples described from the Ethiopian occurrence by Sofiya et al. (2017).

4.3. Magnesite veins and masses

The magnesite in veins and masses is nearly monomineralic and cryptocrystalline. Petrographic, XRD and EDAX analyses indicate that the magnesite veins consist of >98 vol % coarse (0.1-0.4 mm) magnesite with minor amounts of serpentine minerals and iron oxides. The massive magnesite is composed essentially of anhedral fine-grained (0.05-0.1 mm) magnesite (85-90 vol%) with minor serpentine minerals, iron oxides, dolomite and calcite. Carbonate minerals in the magnesite masses display evidence of shearing in the forms of stretched grain ribbons and recrystallized bulges along crystal boundaries. Dolomite and calcite fills cavities and vugs in the magnesite masses is somewhat coarser (0.5-0.8 mm) than magnesite.

4.4. Talc-carbonates

The talc-carbonate rocks occur as massive bodies or sheared mylonitic masses. The massive type consists essentially of carbonate minerals and talc, with minor amounts of amphibole (tremolite, anthophyllite), quartz, chlorite, altered chromian spinel and magnetite. Talc occurs as microcrystalline fibers and fine shreds, or rarely as coarse- to medium-grained flakes. In a few samples, coarse talc flakes occur as nests and open-space filling veins, indicating different generations of talc. Chromian spinel is completely altered to ferritchromite. The mylonitic talc-carbonates consist of carbonate minerals and talc mixed with nodules of

serpentinite and other rock types. Chromian spinel and magnetite occur as highly altered cataclastic and brecciated crystals. In a few samples of mylonitic talc-carbonate, quartz veinlets are observed cutting the talc groundmass.

5. Mineral chemistry

The whole microprobe dataset is given in the Electronic Appendix (Supplementary Tables S1-S8). Not all phases could be analyzed; anthophyllite and tremolite were recognized petrographically but not quantitatively analyzed.

5.1. Olivine

Rare relics of primary olivine can be found in the serpentinites. Microprobe analyses, calculated structural formulae, and end-member components are given in Supplementary Table S1. MgO (48.2-52.4 wt%) and NiO (0.3-0.5 wt%) contents are high, similar to those in primary mantle olivines (e.g. Arai 1980; Takahashi et al. 1987) and other Egyptian ophiolite mantle sequences. Their Fo contents (89.4-93.6; av. 92.1) are clearly distinct from those in olivine from the non-ophiolitic mafic-ultramafic intrusions in Egypt (Fig. 5a).

5.2. Chromian spinel

Electron microprobe analyses and calculated structural formulae of fresh cores and altered rims of chromian spinel are given in Supplementary Tables S2 and S3. In most grains, Al_2O_3, Cr_2O_3 and MgO show a systematic decrease from core to rim, whereas $Fe_2O_3^T$ increases outwards. MnO does not show any systematic variation within fresh spinel cores but is concentrated in the ferritchromite alteration zone in serpentinite samples. The Al–Cr–Fe^{3+} triangular plot reveals differences in chemical composition between various zones, with a well-

developed chemical gap between spinel primary cores and altered rims (Fig. 5b). The fresh cores are rich in Al_2O_3 and Cr_2O_3 and lie along the Cr-Al join. The ferritchromite phase lies close to the Cr-Fe^{3+} join; Al is lost preferentially to Cr. The Cr-magnetite outer rims are nearly devoid of Al_2O_3 and lie along the Cr-Fe^{3+} join with progressive Cr depletion and ferric iron enrichment.

The chromian spinel cores in type-I listwaenite have distinctly higher Mg# (0.5-0.6) than those in serpentinites (Mg# =0.3-0.5) and type-II listwaenite (Mg# =0.3-0.4), with minimal overlap between the populations (Fig. 5c). There are a few large disseminated chromian spinel crystals in the serpentinites with high Mg# (~0.5) cores similar to those recorded in the listwaenite. The interpretation of these Mg# data is discussed below in section 7.3 and is a central part of the argument of this work.

Ferritchromite was analyzed in both serpentinites and listwaenites. The ferritchromite in type I listwaenite is richer in MgO (2.3-4.0 wt%), Al_2O_3 (3.2-4.6 wt%) and Cr_2O_3 (35.3-40.3 wt%) and lower in FeO^T (49.5-55.1 wt%) and MnO (0.6-0.9 wt%) than that in serpentinites (0.4-1.9 wt% MgO, 0.5-1.7 wt% Al_2O_3, 14.0-33.1 wt% Cr_2O_3, 59.0-81.1 wt% FeO^T and 1.1-2.1 wt% MnO) and type II listwaenite (1.0-3.4 wt% MgO, 1.0-2.0 wt% Al_2O_3, 22.0-34.9 wt% Cr_2O_3, 56.1-71.7 wt% FeO^T and 1.0-2.2 wt% MnO). Again, the interpretation of MnO distributions in the spinel family minerals is discussed in section 7.3. Minor but resolvable silica contents are detected in ferritchromite (0.5-1.2 wt% in serpentinite and 0.4-1.3 wt% in listwaenite); silica in the spinel structure has been attributed elsewhere to effects of alteration and metamorphism (Burkhard 1993).

5.3. Mica

Chemical composition and structural formulae of the analyzed muscovite species are given in Supplementary Table S4. Two types of mica can be recognized: fuchsite (green Cr-

311 muscovite) in Type I listwaenite and muscovite (white mica) in Type II listwaenite. Fuchsite in
312 Type-I listwaenite has 6.1-6.3 a.p.f.u Si, which completely overlaps the range of Si in muscovite
313 in the Type-II listwaenite. Fuchsite has higher Cr_2O_3 (1.8-3.7 wt%), FeO^T (2.5-3.7 wt%) and
314 MgO (1.3-2.5 wt%) with lower Al_2O_3 (30.1-32.3 wt%) and K_2O (7.4-9.4 wt%) than muscovite
315 (0.2-0.8 wt% Cr_2O_3, 1.6-2.5 wt% FeO, 1.2-1.6 wt% MgO, 31.8-34 wt% Al_2O_3 and 9.4-10.1 wt%
316 K_2O). Cr_2O_3 contents in fuchsite are negatively correlated with Al_2O_3 contents (Fig. 5d).
317
318 ***5.5. Magnetite***
319 Disseminated magnetite crystals and magnetite rims around chromian spinels could only
320 be analyzed in serpentinite samples; chemical composition and structural formulae are given in
321 Supplementary Table S5. The disseminated magnetite has negligible Cr_2O_3 (0.1-1.3 wt%),
322 whereas the magnetite developed around spinel has Cr_2O_3 contents between 2.0 and 7.8 wt%. On
323 the Cr–Al–Fe^{3+} plot (Fig. 5b), both magnetites plot along the Cr–Fe^{3+} join. Outer Cr-magnetite
324 rims around the ferritchromite in serpentinites are depleted in MnO (0.1-0.9) (see section 7.3
325 below).
326
327 ***5.4. Chlorite***
328 Chlorite was analyzed in serpentinites and both listwaenite types; chemical composition
329 and structural formulae are given in Supplementary Table S6. In the serpentinites, chlorite occurs
330 in two forms, as an aureole around chromian spinel and as isolated sparse crystals in the
331 groundmass. Likewise, in Type I listwaenites, chlorite occurs both intergrown with fuchsite and
332 as disseminated grains. The abundances of SiO_2, Al_2O_3, FeO and Cr_2O_3 in chlorite vary
333 systematically with its mode of occurrence. Chlorite from serpentinites contains higher Al_2O_3
334 (19.3-21.2 wt% in aureoles and 20.0-21.8 wt% in disseminated chlorite) and lower SiO_2 (26.8-

28.2 wt% in aureoles and 27.1-28.8 wt% in disseminated chlorite) than those from listwaenite (16.2-18.8 wt% Al_2O_3 and 28.5-31.0 wt% SiO_2). The chlorite in the aureoles around chromian spinel is Cr-bearing chlorite (kämmererite), with higher Cr_2O_3 (2.5 to 3.9 wt%) and MgO (22.2-23.9 wt%) than the disseminated chlorite (Cr-poor and Fe-rich). Cr-rich chlorite in the serpentinites is classified mainly as ripidolite, whereas the disseminated chlorite includes ripidolite and pycnochlorite (Table S5).

The chlorite intergrowth with fuchsite in the Type I listwaenite is rich in MgO (20.4-22.1 wt%) with somewhat elevated Cr_2O_3 (1.9-2.4 wt%), whereas disseminated chlorite in the Type I listwaenite has elevated FeO^T (18.4-20.3 wt%) and low Cr_2O_3 (1.1-1.6 wt%). According to the classification of Hey (1954), chlorite in Type I listwaenite is classified mainly as pycnochlorite with minor diabantite. Chlorite in Type II listwaenite occurs as sparse crystals and veinlets. Only the veinlet chlorite of veinlets could be analyzed; it has $FeO^T \geq MgO$ and low Cr_2O_3 (<1.2 wt%) and is classified as pycnochlorite and diabantite.

5.5 Talc

A few analyses of talc from serpentinites are given in Supplementary Table S8. Talc has Mg# of 93.3 to 94.8 and analytical totals of 94.3 to 95.2%.

5.6. Carbonates

The results of chemical analyses of carbonate minerals are listed in Supplementary Table S7. The loss of total in the analyzed carbonates is due to CO_2, which is assumed to be present in stoichiometric proportions. The analyses divide the carbonate minerals into magnesite, ferroan magnesite (breunnerite), dolomite and calcite.

Magnesite in serpentinites and Type I listwaenite essentially consists of MgO (45.9-47.5 wt% in serpentinites and 44.7-48.3 wt% in listwaenite), with less than 1.4 wt% CaO. Magnesite in serpentinite contains distinctly higher MnO (1.1-1.4 wt%) than that in Type I listwaenite (0.3-0.7 wt%). Breunnerite is observed in Type I listwaenite; it is defined by significant MgO (39.5-41.3 wt%) and FeO^T (10.3-11.2 wt%) contents with very low concentrations of CaO (<0.9 wt%) and MnO (<0.2 wt%). MgO and FeO^T are negatively correlated among the breunnerite analyses.

Dolomite is observed in serpentinite and in both types of listwaenite. The major components in the analyzed dolomite include MgO (18.7-20.2 wt% in serpentinites, 19.1-19.4 wt% in Type I listwaenite, 19.3-21.0 wt% in Type II listwaenite) and CaO (29.3-30.8 wt% serpentinites, 30.3-31.8 wt% in Type I listwaenite and 29.0-34.6 wt% in Type II listwaenite). Calcite is recorded in both types of listwaenite. It consists essentially of CaO (52.4-57.8 wt%) with minor amounts of MgO (0.4-0.9 wt%) and FeO^T (1.7-1.9 wt%).

6. Geochemistry

Twenty-one samples (9 serpentinites and 12 listwaenitic rocks) were analyzed in order to evaluate the whole-rock geochemical characteristics of the G. Sirsir serpentinized peridotites and listwaenites (Table 1). Serpentinites were selected carefully after rigorous petrographic examination to avoid the presence of any carbonate or quartz veins.

The serpentinites of G. Sirsir have 37.0-40.4 wt% SiO_2, 0.3-1.0 wt% Al_2O_3, 38.3-40.1 wt% MgO, and 6.0-7.6 wt% total Fe as Fe_2O_3 ($Fe_2O_3^T$). Low CaO (<0.8 wt%) contents in the serpentinized peridotite suggest that carbonatization had no effect on these samples, despite their proximity to extensively altered talc-carbonates and listwaenites along nearby shear zones. Serpentinites have high volatile contents (presumed to be mostly H_2O, but including CO_2) based on their LOI values (12.6-15.4 wt%). The high concentrations of Cr (1519-2814 ppm), Ni (1718-

382 2274 ppm), and Co (96-120 ppm) and low concentrations of K_2O (<0.02 wt%) and Na_2O (<0.04
383 wt%) are all consistent with an ultramafic protolith for the serpentinites. Mg# [100 molar
384 $Mg/(Mg+Fe^T)$] of serpentinized peridotites ranges from 90.0 to 92.3 with an average of 91.0. This
385 is generally consistent with oceanic peridotites (Mg# >0.89, Bonatti and Michael 1989) and
386 similar to the Mg# of other reported serpentinites in the Eastern Desert of Egypt (e.g. Azer et al.
387 2013; Khalil et al. 2014; Gahlan et al. 2015; Obeid et al. 2016).

388 The population of listwaenite samples encompasses significant variability in all major
389 oxides, in particular SiO_2, $Fe_2O_3^T$, CaO, MgO, K_2O and volatile contents (LOI). The Type I
390 listwaenites are generally lower in SiO_2 and CaO but higher in Al_2O_3, MgO, $Fe_2O_3^T$, Na_2O, K_2O,
391 and LOI than the Type II listwaenites. The Type I listwaenites are distinctly higher in olivine-
392 compatible trace elements Cr (2147-2765 ppm), Ni (1244-2021 ppm) and Co (51-78 ppm) than
393 the Type II listwaenites (598-1256 ppm Cr, 897-1213 ppm Ni and 28-63 ppm Co).

394 A number of trace elements (V, Ta, Nb, Th and Cs) show no systematic differences
395 between the population of serpentinite samples and either group of listwaenites. However,
396 elevated and variable Rb, Ba and Sr concentrations are only found in listwaenites; these fluid-
397 mobile elements are at or below detection limits in the serpentinites. Au contents are also variable
398 and highly enriched in both Type I (573-2008 ppb) and Type II listwaenites (1502-6584 ppb)
399 compared to serpentinites (4.1-10.7 ppb). Cu, Zn, Pb, Sb, As and Ag are enriched in both types of
400 listwaenites relative to the serpentinites, but the highest values of these elements generally occur
401 in the Type II listwaenites, presumably hosted in the abundant sulfide minerals observed in
402 polished section.

403 Broadly, if we assume that the protoliths of the listwaenites resembled the average
404 serpentinite in bulk composition, then we infer that the alteration and carbonatization processes

were accompanied by significant modification of the whole-rock compositions, as discussed in section 7.4 below.

7. Discussion

7.1. Protolith and geodynamic setting of serpentinites

A variety of tectonic settings for the Egyptian ophiolites has been proposed, including mid-ocean ridge (MOR) and supra-subduction zone (SSZ) environments. Zimmer et al. (1995) assigned a MOR setting based on the geochemistry of the ophiolitic metavolcanic sequences. Other workers have argued that the tectonic setting of Precambrian ophiolites cannot be accurately defined from metavolcanic bulk composition due to the effects of fractional crystallization and subsequent alteration (e.g., Stern et al. 2004; Azer and Stern 2007). More recently, a SSZ tectonic setting has become the consensus view due to detailed work on the mantle sequences, with disagreement focusing on the more detailed question of back-arc (e.g. El Sayed et al. 1999; Ahmed et al. 2001; Farahat et al. 2004; Azer and Khalil 2005) vs. fore-arc (e.g. Azer and Stern 2007; Abd El-Rahman et al. 2009; Azer 2014; Khalil et al. 2014; Gahlan et al. 2015b; Obeid et al. 2016; among others) position.

Relict textures (bastite and mesh) and chromian spinel morphology (Fig. 4) together with high Cr, Ni and Co in the G. Sirsir serpentinized mantle lithologies (Table 1) indicate a depleted, harzburgite-dunite complex protolith. Their low modal abundance of pyroxene (10–15 vol%), low MgO/SiO_2 ratios (<1.04), and low TiO_2 contents (<0.05 wt%) are all features of supra-subduction zone depleted peridotites (e.g. Deschamps et al. 2013; Salters and Stracke 2004). More specifically, their very low CaO (<0.65 wt%) and Al_2O_3 (<0.78 wt%) contents resemble typical fore-arc peridotites (e.g. Ishii et al. 1992) and their very low Al_2O_3/SiO_2 ratios (<0.02) also suggest a forearc setting for the partial melting of the protolith. Serpentinization is thought to

have negligible influence on these indicators, particularly the Al_2O_3/SiO_2 ratio (e.g. Paulick et al. 2006; Deschamps et al. 2013), if quartz veins are avoided.

The chemistry of primary mantle mineral relics such as chromian spinel, olivine and pyroxene can be used as petrogenetic and geodynamic setting indicators to further elucidate the protolith of the serpentinites (e.g., Dick and Bullen 1984; Barnes and Roeder 2001; Ohara et al. 2002; Coish and Gardner 2004; Sobolev and Logvinova 2005; Arif and Jan 2006; Pagé and Barnes 2009; Moghadam et al. 2015; Robinson et al. 2015). The high Cr# (0.61–0.74) (Fig. 5c) with low TiO_2 content (< 0.2 wt%) of relict primary chromian spinel and high Fo content of coexisting olivine (Fo_{89-93}) in both serpentinites and listwaenites argue for a depleted mantle protolith that suffered extensive partial melting in a supra-subduction zone setting, most likely in the fore-arc (Fig. 6) (e.g. Dick and Bullen 1984; Pearce et al. 1984; Ishii et al. 1992; Bloomer et al. 1995; Proenza et al. 2004). This conclusion is consistent with proposed tectonic settings for most Egyptian ophiolites, assigned by a number of recent authors to incorporated fragments of oceanic lithosphere emplaced above a subduction zone in a forearc setting (e.g. Azer and Stern 2007; Abdel-Rahman et al. 2009; Azer et al. 2013; Khalil et al. 2014; Gahlan et al. 2015b).

The Cr# and Al_2O_3 values of spinels are commonly used to constrain the nature of mantle peridotites and the degrees of partial melt extraction they have experienced (Dick and Bullen 1984; Hellebrand et al. 2001). Most studies have found that only the divalent cation contents of chromian spinel are vulnerable to subsolidus re-equilibration during hydrothermal alteration and low-grade metamorphism, such that indicators such as Mg# can suggest faulty petrogenetic interpretations (Mellini et al. 2005; Saumur and Hattori 2013; Singh and Singh 2013; Colás et al. 2014; Qiu and Zhu 2017). Spinels with high Cr# (≥0.6) can be found in residues of high-degree melt extraction and can also crystallize from complementary highly magnesian magmas (Mg-rich tholeiitic or boninitic-type), formed by high-degree partial melting in arc-related tectonic settings

(Dick and Bullen 1984; Zhou et al. 1996; Beccaluva et al. 2004). Based on the empirical equation (F = 10 ln (Cr#) + 24) of Hellebrand et al. (2001), the G. Sirsir peridotite protoliths experienced degrees of partial melt extraction ranging from 19 to 21 %. Such degrees of melting are again consistent with formation in a forearc setting (e.g., Pearce et al. 2000).

The Mg-rich nature of the analyzed olivines (Fo = 89.4-93.4) is similar to mantle olivine in typical fore-arc peridotites that represent residues after extensive melt extraction (e.g. Pearce et al. 2000; Coish and Gardner 2004). The high NiO contents in the analyzed olivines support their primary mantle character (Takahashi et al. 1987). The plot of Cr# of spinel versus Fo content of coexisting olivine relics (Fig. 6) shows the consistency of these two minerals in indicating high degrees of melting and forearc affinity (Uysal et al. 2012), probably representing an early stage of development of a subduction zone (Bonatti and Michael 1989; Bloomer et al. 1995).

7.2. Timing and genetic models of listwaenitization

The serpentinized ultramafics from ophiolitic mantle sections in the Eastern Desert of Egypt are in many cases conspicuously altered and the alteration products provide valuable indicators for mineral exploration. Alteration is attributed to the effects of circulation and infiltration by hydrothermal fluids which can, depending on fluid composition and temperature, produce various assemblages including serpentinite, listwaenite and talc-carbonate rock. However, the timing of this alteration — relative to other events in the formation and obduction of oceanic crust — is controversial. The origin of fluids that drove alteration of the ANS ophiolites is unclear as well (e.g., Newton and Stern 1990; Stern and Gwinn 1990; Azer 2013; Boskabadi et al. 2017; Hamdy and Gamal El Dien 2017), having been attributed variously to: (1) mantle-derived CO_2-bearing fluids during near-ridge oceanic crust formation (e.g. Lebda 1995; Boskabadi et al. 2017; Hamdy and Gamal El Dien 2017); and (2) meteoric and metamorphic

hydrothermal fluids penetrating along tectonic fractures during or even after exhumation to upper crustal levels (e.g. Shukri and Lutfi 1959; Salem et al. 1997; Ghoneim et al. 1999, 2003; Hamdy and Lebda 2007). In fact, systematic stable isotope (C, O, H) studies are generally needed to distinguish the temperature of alteration and the composition and source of the metasomatic agents (Fallick et al. 1991; Zedef et al. 2000; Mirnejad et al. 2008; Bjerga et al. 2015; Boskabadi et al. 2017)

In the study area, all occurrences of both Type I and Type II listwaenites are structurally controlled by faults and shear zones, indicating a close link between alteration and the tectonic evolution, metamorphism and regional geology of the area. Although Abdeen et al. (2008) comprehensively discussed the tectonic evolution of the G. Sirsir area, the position of listwaenite formation in this tectonic evolution has not been considered before. Deformation and schistosity in the Type I listwaenites indicate that the listwaenitization was contemporaneous with serpentinization. On the other hand, the absence of deformation in the Type II listwaenites and their spatial association with nearby granites suggests that they postdate serpentinization.

The fluid CO_2 activity and temperature ranges necessary to drive replacement reactions of the silicates in ultramafic rocks (forsteritic olivine and enstatite-rich orthopyroxene) with carbonates (principally magnesite) has been reviewed by a number of authors, including the experimental study of Saldi et al. (2012) and Falk and Kelemen's (2015) study of listwaenite along the basalt thrust of the Samail Ophiolite, Oman. The reader is referred to those references for detailed thermodynamic and kinetic discussions.

The structurally distinct deformed (Type I) and undeformed (Type II) listwaenites are also compositionally (Table 1) and mineralogically (Fig. 4) distinct. Type I listwaenite has higher MgO values due to the presence of magnesite as the most common carbonate mineral and high

values of $Fe_2O_3^T$ hosted by ferroan magnesite (breunnerite). The clear enrichment of this group in K_2O, Na_2O, and Al_2O_3 (1.5-2.2 wt%) reflects the presence of a potassium bearing phase, fuchsite.

The correlation of structurally and compositionally distinct types indicates that hydrothermal listwaenitization took place through two metasomatic stages. The first metasomatic stage was coincident with serpentinization of the original residual peridotites and so likely took place during the development of the ophiolite sequence as fore-arc oceanic crust near a spreading center (~750-700 Ma). In near-ridge settings, penetrative serpentinization of the uppermost mantle section is thought to be driven by magmatic hydrothermal systems fed by seawater-derived hydrous fluids that gain buoyancy as they are drawn inwards and downwards towards sites of focused upwards discharge. However, noting that forearc settings in particular are positioned above the accretionary prism of a subduction zone, in such cases there is an additional source of CO_2-rich fluids, generated below the oceanic crust by decomposition of subducted, carbonate-bearing sedimentary rocks at high temperature. These buoyant CO_2-rich fluids infiltrate upwards along fractures and fault planes and can develop a magnesite-talc-quartz-fuchsite (listwaenite) mineral paragenesis locally. As far as can be reconstructed from the coincidence of serpentinite and massive magnesite textures, these two fluid infiltrations — penetrative seawater from above and focused CO_2-rich fluid from below — occurred simultaneously. In the areas transformed to listwaenite at this stage, all the mafic silicates, primary or secondary, that might later exchange with chromian spinel are removed. Hence, despite a protracted history of cooling after this stage, the Mg# of chromian spinel in listwaenite is not affected by any temperature-sensitive changes in Mg–Fe^{2+} distribution coefficients between spinel and mafic silicates. On the other hand, the Mg# of chromian spinel in the host serpentinites continuously evolves by sub-solidus Mg–Fe^{2+} exchange with mafic silicates as the section of oceanic lithosphere cools and ages.

524 The second metasomatic stage then took place during the East and West Gondwana
525 continental collision (~650–600 Ma) marked in the field area by development of the Najd fault
526 system and granitic intrusions. During this stage, the Type II listwaenites formed along shear
527 zones from serpentinites bearing chromian spinels whose divalent cation contents had already
528 been reset over the ~100 Ma of subsolidus evolution since their emplacement. Fluids introduced
529 at this stage were highly oxidizing and contributed to oxidation of relict chromian spinel to form
530 ferritchromite and/or Cr- magnetite in both serpentinites and listwaenites.
531
532 ***7.3. Chromian spinel alteration***
533 It is rare for disseminated chromian spinels found in Egyptian ophiolites to preserve
534 zoning profiles in their distributions of Al, Fe^{3+} and Cr or of Mg, Fe^{2+}, and Mn (e.g. Ahmed et al.
535 2001; Farahat 2008; Azer 2014; Gahlan et al. 2015b; Abdel-Karim and El-Shafei 2017). This
536 suggests an unfortunate gap between the timescales of trivalent and divalent ion redistribution in
537 spinel, with timescales of trivalent ion diffusion generally longer than orogenic events and of
538 divalent ion diffusion generally shorter than events. Nearly complete modification of divalent
539 element distributions during alteration and metamorphism complicates the use of spinel as a
540 petrogenetic indicator (e.g. Barnes and Roeder 2001; Gonzálea-Jimènez et al. 2009; Proenza et al.
541 2008; Zhou et al. 1996). However, listwaenite presents a special case. The Mg–Fe^{2+} exchange
542 that can occur in serpentinites is arrested in listwaenite because spinel does not readily exchange
543 with carbonate minerals. The chromian spinels in Type I listwaenite are homogeneous in the
544 cores. We argue that the common preservation of unaltered chromian spinel cores with high Mg#
545 in type I listwaenite implies preservation of high-temperature signatures in the chromian spinel of
546 listwaenite due to early carbonation.

However, Mg# in the chromian spinel cores of Type II listwaenites more closely resembles the values in the serpentinites. This is attributed to ongoing equilibration between chromian spinel and surrounding silicate as the serpentinite protoliths of the listwaenite-like rocks followed the same cooling path as the serpentinites until later carbonate alteration.

Low-temperature serpentinization produces ferritchromite zones with, in the Type II listwaenites, magnetite outer zones, as a result of fluid ingress along cracks and around the grain boundaries of Cr-spinel. During the ferritchromite formation Fe and to a lesser extent Mn are introduced into Cr-spinel, while Al, Mg and Cr diffuse outward. Hence ferritchromite rims have higher Cr/(Cr+Al) and lower Mg/(Mg+Fe^{2+}) than unaltered cores. The depletion of MnO in ferritchromite of Type I listwaenite can be attributed to the presence of carbonate minerals, a favorable sink for Mn (Deer et al. 1992). This indicates that the ferritchromite formed after carbonatization of Type I listwaenites but before carbonatization of Type II listwaenites. The absence of Cr-magnetite around the ferritchromite zone of chromian spinel in the Type I listwaenites indicates that the ferritchromite did not re-equilibrate with the surrounding silicates, and consequently Cr-magnetite is absent.

Sofiya et al. (2017) studied listwaenite formed by replacement of serpentinite in the Tulu Dimtu tectonic mélange in Ethiopia, about 1500 km further south along the East African Orogen belt than the G. Sirsir study area. Their petrographic description makes no mention of fuchsite and it appears that all the listwaenite sampled by those authors resembles the Type II listwaenite defined here. Indeed, based on the Mg# of chromian spinel in the Ethiopian case, Sofiya et al. (2017) reach a similar conclusion to ours about the timing of spinel equilibration compared to carbonatization. However, the absence of Type I samples in the Ethiopian case means there is no evidence for the first stage of fluid infiltration at that locality.

570 Kämmererite is not typically an important product of serpentinization. Its presence in the
571 current suite may instead reflect replacement of chromian spinel during later alteration or regional
572 metamorphism. The significant Cr content of kämmererite and its petrographic relationship to
573 primary relics of Cr-spinel suggest this type of chlorite forms after primary chromian spinel,
574 perhaps during its alteration to ferritchromite. During alteration of chromian spinel, most Cr and
575 Fe enter into ferritchromite, whereas Al and Mg are released to the surrounding silicate minerals.
576 The excess Al and Cr react with serpentine minerals to produce kämmererite (Azer and Stern
577 2007). Cr-chlorite aureoles are not observed in the Type I listwaenites because the carbonates
578 prevent exchange of Cr with mafic silicate minerals.
579
580 ***7.4. Element mobility during serpentinization and listwaenitization: Application***
581 The chemical changes during the different styles of serpentinite alteration into listwaenite
582 and talc-carbonate rocks are dominated by the addition and removal of CO_2 and H_2O and by the
583 redistribution of SiO_2, MgO and CaO accompanying growth of carbonate minerals at the expense
584 of silicates. Although Mg^{2+} and Ca^{2+} can be leached during hydrous fluid alteration, the high
585 activity of CO_2 in the present case instead stabilizes Mg- and Ca-carbonate phases that reduce the
586 mobility and loss of these cations. Alteration also caused redistribution of trace elements, with
587 some being locally remobilized within the rock, some being added from a fluid phase, and others
588 being leached out of the rock. Serpentinites were enriched in fluid-mobile elements (K, As, Rb,
589 Sr, Sb, Cs, Ba, Pb, and U) relative to primitive (McDonough and Sun 1995) or depleted mantle
590 values (Salters and Stracke 2004), first due to modification in the mantle wedge (e.g. Hattori and
591 Guillot 2003, 2007; Deschamps et al. 2011, 2012) and perhaps also from serpentinizing fluids; in
592 any case they were retained in the serpentine minerals (Deschamps et al. 2013). Both types of

593 listwaenite show further enrichment of these elements, suggesting both efficient retention by the
594 carbonates and additional contribution from the CO_2-rich alteration fluid.

595 Listwaenite rocks have long been considered an indicator of Au mineralization, although
596 the relationship between Au enrichment and listwaenite formation is still unclear. Gold shows
597 similar behavior, to some extent, to the fluid-mobile elements. Its concentrations in the G. Sirsir
598 serpentintes are commonly higher than in typical serpentinized mantle peridotite (i.e. ~3–5 ppb;
599 Buisson and Leblanc 1987), average ophiolitic rocks (i.e. ~2.8 ppb; Foster 1991), or depleted
600 mantle (i.e. ~1 ppb; Salters and Stracke 2004). Compared to serpentinites, the listwaenite rocks of
601 the G. Sirsir then show much higher concentrations of Au (673-2008 ppb in Type I listwaenites
602 and 987-6584 ppb in Type II listwaenites), suggesting that intense alteration of the serpentinites
603 to form listwaenite within shear zones was accompanied by fluid concentration that enriched
604 these rocks in Au (as well as As and Ag).

605 The current results are comparable to other studies worldwide that have demonstrated
606 hosting of Au mineralization in listwaenite (e.g. Buisson and Leblanc 1985, 1986, 1987; Ash and
607 Arksey 1990; Aydal 1990; Koç and Kadıolu 1996; Uçurum and Larson 1999; Uçurum 2000;
608 Belogub et al. 2017) as well as specifically within the Eastern Desert of Egypt (Botros 1993,
609 2002; Osman 1995; Oweiss et al. 2001; Ramadan et al. 2005; Zoheir and Lehmann 2011; Azer
610 2013). Some authors have argued that the relation between gold mineralization, listwaenitization
611 and shear zones reflects their combination of weak shear strength and high permeability, in strong
612 rheological contrast with more coherent rocks such as the granitoids commonly found in contact
613 with listwaenites in ANS gold deposits (e.g. Buisson and Leblanc 1987; Zoheir and Lehmann
614 2011; Azer 2013; Zoheir and Moritz 2014).

615

616 ***7.5. Chlorite geothermometry***

Compositions of chlorite are sensitive to prevailing physicochemical conditions during its formation because distribution coefficients between precursor ferromagnesian minerals and chlorite vary, especially as a function of temperature. Therefore, the chemical composition of chlorite has been used to determine the temperature of its formation by replacement reactions (e.g. Kranidiotis and MacLean 1987; Cathelineau and Nieva 1985; Cathelineau 1988; Hillier and Velde 1991; Bourdelle et al. 2013; Bourdelle and Cathelineau 2015; Yavuz et al. 2015). Kranidiotis and MacLean (1987) corrected the linear correlation shown by Cathelineau and Nieva (1985) between tetrahedral Al and temperature in chlorites saturated with an Al-rich phase with as estimate of the effect of Fe/(Fe+Mg) on the temperature. The resulting equation is suitable for chlorite that coexists with aluminous spinel or muscovite. The opposite, Al-undersaturated boundary of the chlorite stability field lies about 50 °C higher; given the presence of Cr in the coexisting spinels and muscovites in most of the analyzed rocks, it is possible that the Kranidiotis and MacLean (1987) thermometer systematically underestimates chlorite temperatures in these rocks by ~10 °C. The calculated temperatures for chlorite formation according to the geothermometer equation of Kranidiotis and MacLean (1987) are listed in Supplementary Table S6; the equation is given as a footnote to the Table. The temperatures obtained are higher in serpentinites (286-311 ^{o}C in aureoles and 277-300 ^{o}C in disseminated chlorite) than in Type I listwaenite (243-274 in chlorite associated with fuchsite and 229-270 ^{o}C in disseminated chlorite) or Type II listwaenite-like rock (233-249 ^{o}C). Interestingly, Fe-rich chlorites in Type II listwaenite-like rocks give the lowest temperature range (av. 240°C), suggesting they sample a unique hydrothermal stage, likely the last to affect the G. Sirsir bodies.

Zoheir (2011) obtained quite similar temperatures (~270–340 °C) for chlorite in listwaenite in south Eastern Desert of Egypt. We note that the chlorite temperatures from both our study and that of Zoheir (2011) are plainly higher than the inferred maximum temperatures of

641 ~65 ^{o}C for listwaenite formation proposed by Wilde et al. (2002) or the magnesite clumped
642 isotope temperatures of 65-114 °C for Oman ophiolite basal listwaenite inferred by Falk and
643 Kelemen (2015), whereas they are much more similar to temperatures estimated by numerous
644 authors for other listwaenites worldwide (e.g., Andrew, 1985; Buisson and Leblanc, 1987; Weir
645 and Kerrick, 1987; Madu et al.,1990; Spiridonov, 1991; Schandl and Wicks, 1993; Schandl and
646 Gorton, 2012; Oskierski et al., 2013).
647

648 **8. Implications**

649 The G. Sirsir Serpentinized ultramafics form tectonic sheets and lenses within a tectonic
650 mélange, elongated in the NW–SE direction. They are extensively altered along thrust and shear
651 zones into quartz-carbonate rocks (listwaenite assemblages) and talc-carbonates. Chromian spinel
652 relics in both serpentinites and listwaenites apparently preserve pristine ratios of trivalent cations,
653 with high Cr# typical of spinel in residual peridotites. However, relict chromian spinel in the
654 Type I listwaenite has significantly higher Mg# and lower MnO than that of serpentinites,
655 suggesting nearly complete alteration of ultramafic rocks to form listwaenite took place prior to
656 re-equilibration between chromian spinel and the surrounding mafic minerals in serpentinites.
657 The lower Mn-content of ferritchromite rims in the listwaenites compared to the serpentinites
658 indicates this stage of spinel alteration also postdates carbonatization in the listwaenites, since
659 carbonate minerals are favorable sinks of Mn.

660 Based on field and textural observations, it is very likely that carbonation affected
661 serpentinites through two stages to form the two types of listwaenites. The first stage was
662 apparently contemporaneous with serpentinization and emplacement of the mantle section of the
663 G. Sirsir ophiolite into oceanic lithosphere. The second stage (~650-620 Ma), forming the
664 unsheared Type II listwaenite-like rocks, is younger than the presumed protolith age and

665 associated with the Najd fault system, collisional tectonics, and ophiolite obduction. The
666 implication is that both these stages of deformation were associated with infiltration of CO_2-rich
667 fluids. Carbonate source rocks likely decomposed to release such fluids both from the slab
668 underlying the original forearc setting of spreading and ophiolite formation and again in the
669 footwall of the structures that accommodated ophiolite obduction onto a continental shelf. At
670 some level, then, both stages of listwaenitization and associated Au mineralization can be traced
671 to the tropical setting of the Mozambique Ocean and the resulting abundance of carbonate
672 sediments in the marine sequences trapped within the Pan-African orogeny.
673

674 **Acknowledgements**

675 MKA's visit to the California Institute of Technology was supported by the US Agency
676 for International Development Cairo Initiative. PDA acknowledges support from the US National
677 Science Foundation, award EAR-1551433. This work was supported partly by King Saud
678 University, Deanship of Scientific Research, Research Group No (RG-1436-036).
679

680 **References**

681 Abd El-Rahman, Y., Helmy, H.M., Shibata, T., Yoshikawa, M., Arai, S., and Tamura, A. (2012)
682 Mineral chemistry of the Neoproterozoic Alaskan-type Akarem Intrusion with special
683 emphasis on amphibole: Implications for the pluton origin and evolution of subduction-
684 related magma. Lithos, 155, 410−425.
685 Abd El-Rahman, Y., Polat, A., Dilek, Y., Fryer, B.J., El-Sharkawy, M. and Sakran, S. (2009)
686 Geochemistry and tectonic evolution of the Neoproterozoic incipient arc-fore-arc crust in
687 the Fawakhir area, Central Eastern Desert of Egypt. Precambrian Research, 175, 116–134.

688 Abdeen, M.M., Sadek, M.F., and Greiling, R.O. (2008) Thrusting and multiple folding in the
689 Neoproterozoic Pan-African basement of Wadi Hodein area, south Eastern Desert, Egypt.
690 Journal of African Earth Sciences, 52, 21–29.
691 Abdel-Karim, A.M. and El-Shafei, S.A. (2017) Mineralogy and chemical aspects of some
692 ophiolitic metaultramafics, central Eastern Desert, Egypt: Evidences from chromites,
693 sulphides and gangues. Geological Journal (published online: DOI: 10.1002/gj.2914).
694 Ahmed, A.H., Arai, S., and Attia, A.K. (2001) Petrological characteristics of podiform
695 chromitites and associated peridotites of the Pan African ophiolite complexes of Egypt.
696 Mineralium Deposita, 36, 72-84.
697 Ali, K.A., Azer, M.K., Gahlan, H.A., Wilde, S.A., Samuel, M.D., and Stern, R.J. (2010) Age
698 constraints on the formation and emplacement of Neoproterozoioc ophiolites along the
699 Allaqi-Heiani suture, South Eastern Desert of Egypt. Gondwana Research, 18, 583–595.
700 Andrew, K. (1985) Fluid inclusion and chemical studies of gold-quartz veins in the Atlin Camp,
701 Northwestern British Columbia. B.Sc. thesis, Univ. British Columbia, Vancouver, BC,
702 Canada. 116 pp.
703 Arai, S. (1980) Dunite-harzburgite-chromitite complexes as refractory residue in the Sangun-
704 Yamaguchi zone, western Japan. Journal of Petrology, 21, 141-165.
705 Arai, S. (1992) Chemistry of chromian spinel in volcanic rocks as a potential guide to magma
706 chemistry. Mineralogical Magazine 56, 173-184.
707 Arai, S. (1994) Characterization of spinel peridotites by olivine-spinel compositional
708 relationships: Review and interpretations. Chemical Geology, 113, 191-204.
709 Arif, M. and Jan, M.Q. (2006) Petrotectonic significance of the chemistry of chromite in the
710 ultramafic-mafic complexes of Pakistan. Journal of Asian Earth Sciences, 27, 628–646.

711 Ash, C.H. and Arksey, R.L. (1990) The listwanite-lode gold association in British Columbia.
712 Geological Survey Branch, Geological Fieldwork 1989, Paper 1990-1, 359-364.
713 Aydal, D. (1990) Gold-bearing listwaenites in the Arac Massif, Kastamonu, Turkey. Terra Nova,
714 2, 43-52.
715 Azer, M.K. (2013) Evolution and economic significance of listwaenites associated with
716 Neoproterozoic ophiolites in south Eastern Desert, Egypt. Geologica Acta, 11(1), 113–
717 128.
718 Azer, M.K. (2014) Petrological studies of Neoproterozoic serpentinized ultramafics of the Nubian
719 Shield: Spinel compositions as evidence of the tectonic evolution of the Egyptian
720 ophiolites. Acta Geologica Polonica, 64, 113–127.
721 Azer, M.K. and Khalil, A.E.S. (2005) Petrological and mineralogical studies of Pan-African
722 serpentinites at Bir Al-Edeid area. Central Eastern Desert, Egypt. Journal of African Earth
723 Sciences, 43, 525-536.
724 Azer, M.K. and Stern, R.J. (2007) Neoproterozoic (835-720 Ma) serpentinites in the Eastern
725 Desert, Egypt: Fragments of fore-arc mantle. The Journal of Geology, 115, 457-472.
726 Azer, M.K. and El-Gharbawy, R.I. (2011) Contribution to the Neoproterozoic layered mafic-
727 ultramafic intrusion of Gabal Imleih, south Sinai, Egypt: Implication of post-collisional
728 magmatism in the north Arabian-Nubian Shield. Journal of African Earth Sciences, 60,
729 253-272.
730 Azer, M.K., Samuel, M.D., Ali, K.A., Gahlan, H.A., Stern, R.J., Ren, M., and Moussa, H.E.
731 (2013) Neoproterozoic ophiolitic peridotites along the Allaqi-Heiani Suture, South
732 Eastern Desert, Egypt. Mineralogy and Petrology, 107, 829–848.

733 Azer, M.K., Obeid, M.A., and Gahlan, H.A. (2016) Late Neoproterozoic layered mafic intrusion
734 of arc-affinity in the Arabian-Nubian Shield: A case study from the Shahira layered mafic
735 intrusion, southern Sinai, Egypt. Geologica Acta, 14, 237-259.
736 Azer, M.K., Gahlan, H.A., Asimow, P.D., and Al-Kahtany, K.M. (2017) The Late
737 Neoproterozoic Dahanib mafic-ultramafic intrusion, South Eastern Desert, Egypt: is it an
738 Alaskan-type or a layered intrusion? American Journal of Science, 317, 901–940.
739 Barnes, S. J. and Roeder, P. L. (2001) The Range of Spinel Compositions in Terrestrial Mafic and
740 Ultramafic Rocks. Journal of Petrology, 42, 2279–2302.
741 Beccaluva, L., Coltori, M., Giunta, G., and Siena, F. (2004) Tethyan vs. Cordilleran ophiolites: a
742 reappraisal of distinctive tectono-magmatic features of supra-subduction complexes in
743 relation to subduction mode. Tectonophysics, 393, 163-174.
744 Belogub, E.V., Melekestseva, I. Y., Novoselov, K. A., Zabotina, M. V., Tret'yakov, G. A.,
745 Zaykov, V. V., and Yuminov, A. M. (2017) Listvenite-related gold deposits of the South
746 Urals (Russia): A review. Ore Geology Reviews, 85, 247–270.
747 Bjerga, A., Konopásek, J., and Pedersen, R. B. (2015) Talc–carbonate alteration of ultramafic
748 rocks within the Leka Ophiolite Complex, Central Norway. Lithos, 227, 21–36.
749 Bloomer, S. H., Taylor, B., MacLeod, C. J., Stern, R. J., Fryer, P., Hawkins, J. W., and Johnson,
750 L. (1995) Early arc volcanism and ophiolite problem: A perspective from drilling in the
751 Western Pacific. In: Taylor, B. and Natland, J. (Eds.), Active Margins and Marginal
752 Basins of the Western Pacific, Geophysical Monograph, Vol. 88. American Geophysical
753 Union, Washington, DC, pp. 1–30.
754 Bonatti, E., and Michael, P. J. (1989) Mantle peridotites from continental rifts to ocean basins to
755 subduction zones. Earth and Planetary Science Letters, 91, 297–311.

Boskabadi, A., Pitcairn, I. K., Broman, C., Boyce, A., Teagle, D. A. H., Cooper, M. J., Azer, M. K., Mohamed, F. H., Stern, R. J., and Majka, J. (2017) Carbonate alteration of ophiolitic rocks in the Arabian–Nubian Shield of Egypt: sources and compositions of the carbonating fluid and implications for the formation of Au deposits. International Geology Review, 59(4), 391–419.

Botros, N.S. (1993) New prospects for gold mineralization in Egypt. Annals of Geological Survey of Egypt, 19, 47–56.

Botros, N.S. (2002) Metallogeny of gold in relation to the evolution of the Nubian Shield in Egypt. Ore Geology Review, 19, 137–164.

Botros, N.S. (2004) A new classification of the gold deposits of Egypt. Ore Geology Reviews, 25, 1-37.

Bourdelle, F. and Cathelineau, M. (2015) Low-temperature chlorite geothermometry: a graphical representation based on a T–R2+–Si diagram. European Journal of Mineralogy, 27, 617–626.

Bourdelle, F., Parra, T., Chopin, C., and Beyssac, O. (2013) A new chlorite geothermometer for diagenetic to low-grade metamorphic conditions. Contributions to Mineralogy and Petrology, 165, 723–735.

Buisson, G. and Leblanc, M. (1985) Gold in carbonatized ultramafic rocks from ophiolite complexes. Economic Geology, 80, 2026-2029.

Buisson, G. and Leblanc, M. (1986) Gold-bearing listwaenites (carbonatized ultramafic rocks) from ophiolite complexes. In: Gallagher, J.M., Ixer, R.A., Neary, C.R. (eds.). Metallogeny of Basic and Ultrabasic Rocks. London, Institution of Mining and Metallurgy, 121-132.

Buisson, G. and Leblanc, M. (1987) Gold in mantle peridotites from Upper Proterozoic ophiolites in Arabia, Mali, and Morocco. Economic Geology, 82, 2091-2097.

780 Burkhard, D.J.M. (1993) Accessory chromium spinels: their coexistence and alteration in
781 serpentinites. Geochimica Cosmochimica Acta, 57, 1297–1306.
782 Cathelineau, M. (1988) Cation site occupancy in chlorites and illites as a function of temperature.
783 Clay Minerals, 23, 471-485.
784 Cathelineau, M. and Nieva, D. (1985) A chlorite solid solution geothermometer. The Los Azufrez
785 (Mexico) geothermal system. Contributions to Mineralogy and Petrology, 91, 235–244.
786 Coish, R.A. and Gardner, P. (2004) Suprasubduction-zone peridotite in the northern USA
787 Appalachians: evidence from mineral composition. Mineralogical Magazine, 68, 699–
788 708.
789 Colás, V., González-Jiménez, J. M., Griffin, W. L., Fanlo, I., Gervilla, F., O'Reilly, S. Y.,
790 Pearson, N. J., Kerestedjian, T., and Proenza, J. A. (2014) Fingerprints of metamorphism
791 in chromite: new insights from minor and trace elements. Chemical Geology, 389, 137–
792 152.
793 De Caritat, P., Hutcheon, I., and Walsche, J. L. (1993) Chlorite geothermometry: a review. Clays
794 and Clay Minerals, 41, 219–239.
795 Deer, W. A., Howie, R. A., and Zussman, J. (1992) An introduction to the rock forming minerals.
796 Second Edition, Longman Scientific and Technical, London, 696pp.
797 Deschamps, F., Guillot, S., Godard, M., Andreani, M., and Hattori, K. H. (2011) Serpentinites act
798 as sponges for fluid-mobile elements in abyssal and subduction zone environments. Terra
799 Nova, 23, 171–178.
800 Deschamps, F., Godard, M., Guillot, S., Chauvel, C., Andreani, M., Hattori, K., Wunder, B., and
801 France, L. (2012) Behavior of fluid-mobile elements in serpentines from abyssal to
802 subduction environments: Examples from Cuba and Dominican Republic. Chemical
803 Geology, 312-313, 93–117.

804 Deschamps, F., Godard, M., Guillot, S., and Hattori, K. (2013) Geochemistry of subduction zone
805 serpentinites: A review. Lithos, 178, 96-127.
806 Dick, H. J. B., and Bullen, T. (1984) Chromian spinel as a petrogenetic indicator in abyssal and
807 Alpine-type peridotites and spatially associated lavas. Contributions to Mineralogy and
808 Petrology, 86, 54–76.
809 El Bayoumi, R.M. (1983) Ophiolites and mélange complex of Wadi Ghadir area, Eastern Desert,
810 Egypt. Bulletin of Faculty of Science, King Abdul Aziz University, 6, 329–342.
811 El Sayed, M. M., Furnes, H., and Mohamed, F. H. (1999) Geochemical constraints on the
812 tectonomagmatic evolution of the late Precambrian Fawakhir ophiolite, Central eastern
813 Desert, Egypt. Journal of African Earth Sciences, 29, 515-533.
814 El Sharkawy, M. A., and E1 Bayoumi, R. M. (1979) The ophiolites of Wadi Ghadir area, Eastern
815 Desert, Egypt. Annals of the Geological Survey of Egypt, 9, 125–135.
816 Falk E. S. and Kelemen P. B. (2015) Geochemistry and petrology of listvenite in the Samail
817 ophiolite, Sultanate of Oman: Complete carbonation of peridotite during ophiolite
818 emplacement. Geochimica et Cosmochimica Acta, 160, 70-90.
819 Fallick A. E., Ilich M., and Russell M. J. (1991) A stable isotope study of the magnesite deposits
820 associated with the Alpine-type ultramafic rocks of Yugoslavia. Economic Geology, 86,
821 847–861.
822 Farahat, E. S. (2008) Chromian-spinels in serpentinites and talc carbonates of the El Ideid-El-
823 Sodmein District, central Eastern Desert, Egypt: their metamorphism and petrogenetic
824 implications. Chemie der Erde, 68, 193-205.
825 Farahat, E. S., and Helmy, H. M. (2006) Abu Hamamid Neoproterozoic Alaskan-type complex,
826 south Eastern Desert, Egypt. Journal of African Earth Sciences, 45,187–197.

827 Farahat, E. S., El Mahalawi, M. M., and Hoinkes, G. (2004) Continental back-arc basin origin of
828 some ophiolites from the Eastern Desert of Egypt. Mineralogy and Petrology, 82, 81-104.
829 Gahlan H., Arai S., and Almadani, S. (2015) Petrogenesis of carbonated meta-ultramafic lenses
830 from the Neoproterozoic Heiani ophiolite, South Eastern Desert, Egypt : A natural
831 analogue to CO_2 sequestration. Journal of African Earth Sciences, 102, 102–115.
832 Gahlan H., Azer M., and Khalil A. E. S. (2015b) The Neoproterozoic Abu Dahr ophiolite, South
833 Eastern Desert, Egypt: petrological characteristics and tectonomagmatic evolution.
834 Mineralogy and Petrology, 109, 611–630.
835 Ghoneim, M. F. (1989) Mineral chemistry of some gabbroic rocks of the central Eastern Desert,
836 Egypt. Journal of African Earth Sciences, 9, 289–295.
837 Ghoneim, M. F., Salem, I.A., and Hamdy, M. M. (1999) On the petrogenesis of magnesite from
838 Gebel El-Maiyit, central Eastern Desert, Egypt. Fourth International Conference on the
839 Geology of the Arab World, 1, 575-593.
840 Ghoneim, M. F., Salem, I. A., and Hamdy, M. M. (2003) Origin of magnesite veins in
841 serpentinites from Mount El-Rubshi and Mount El-Maiyit, Eastern Desert, Egypt.
842 Archiwum Mineralogiczne, 54, 41-63.
843 González-Jiménez, J. M., Kerestedjian, T., Proenza, J. A., and Gervilla, F. (2009) Metamorphism
844 on chromite ores from the Dobromirtsi Ultramafic Massif, Rhodope Mountains (SE
845 Bulgaria). Geologica Acta, 7, 413-429.
846 Halls, C. and Zhao, R. (1995) Listwaenite and related rocks: perspectives on terminology and
847 mineralogy with reference to an occurrence at Cregganbaun, Co. Mayo, Republic of
848 Ireland. Mineralium Deposita, 30, 303–313.

849 Hamdy, M.M. and Lebda E.M. (2007) Metamorphism of ultramafic rocks at Gebel Arais and
850 Gebel Malo Grim, Eastern Desert, Egypt: mineralogical and O-H stable isotopic
851 constraints: Egyptian Journal of Geology, 51, 105-124.
852 Hamdy, M. M. and Gamal El Dien, H. M. (2017) Nature of serpentinization and carbonation of
853 ophiolitic peridotites (Eastern Desert, Egypt): constrains from stable isotopes and whole
854 rock geochemistry. Arabian Journal of Geoscience (published online: DOI
855 10.1007/s12517-017-3215-6).
856 Harraz, H. Z. (2000) A genetic model for a mesothermal Au deposit: Evidence from fluid
857 inclusions and stable isotopic studies at El Sid gold mine, Eastern Desert, Egypt. Journal
858 of African Earth Sciences, 30, 267–282.
859 Hattori, K. H. and Guillot, S. (2003) Volcanic fronts form as a consequence of serpentinite
860 dehydration in the forearc mantle wedge. Geology, 31(6), 525–528.
861 Hattori, K. H. and Guillot, S. (2007) Geochemical character of serpentinites associated with high-
862 to ultrahigh-pressure metamorphic rocks in the Alps, Cuba, and the Himalayas: Recycling
863 of elements in subduction zones. Geochemistry, Geophysics, Geosystems, 8, 9.
864 Hellebrand, E., Snow, J. E., Dick, H. J. B., and Hoffmann, A. W. (2001) Coupled major and trace
865 elements as indicators of the extent of melting in mid-Ocean ridge peridotites. Nature,
866 410, 677–681.
867 Helmy, H. M. and El Mahallawi, M. M. (2003) Gabbro Akarem mafic-ultramafic complex,
868 Eastern Desert, Egypt: a Late Precambrian analogue of Alaskan-type complex.
869 Mineralogy and Petrology, 77, 85–108.
870 Hey, M. H. (1954) A new review of the chlorites. Mineralogical Magazine, 30, 272-292.
871 Hillier, S., and Velde, B. (1991) Octahedral occupancy and the chemical composition of
872 diagenetic (low-temperature) chlorites. Clay Minerals, 26, 149–168.

873 Ishii, T., Robinson, P. T., Maekawa, H., and Fiske, R. (1992) Petrological studies of peridotites
874 from diapiric Serpentinite Seamounts in the Izu- Ogasawara-Mariana forearc, leg 125. In:
875 J. Pearce, L. B. Stokking, et al. (Eds.), Proceedings of the Ocean Drilling Project, Leg
876 125, Scientific Results (College Station), pp. 445-485.
877 Jarrar, G., Stern, R. J., Saffarini, G., and Al-Zubi, H. (2003) Late- and post-orogenic
878 Neoproterozoic intrusions of Jordan: implications for crustal growth in the northernmost
879 segment of the East African orogen. Precambrian Research, 123, 295-319.
880 Johnson, P. R. and Woldehaimanot, B. (2003) Development of the Arabian-Nubian Shield:
881 Perspectives on accretion and deformation in the northern East African Orogen and the
882 assembly of Gondwana. In: M., Yoshida, S., Dasgupta and B., Windley (Eds.),
883 Proterozoic East Gondwana: Supercontinent assembly and breakup. Geological Society of
884 London Special Publications, 206, 289-325.
885 Kelemen, P. B., Matter, J., Streit, E. E., Rudge, J. F., Curry, W. B., and Bluztajn, J. (2011) Rates
886 and mechanisms of mineral carbonation in peridotite: Natural processes and recipes for
887 enhanced, in situ CO_2 capture and storage: Annual Review of Earth and Planetary
888 Sciences, 39, 545–576.
889 Khalil, A. E. S. and Azer, M. K. (2007) Supra-subduction affinity in the Neoproterozoic
890 serpentinites in the Eastern Desert, Egypt: Evidence from mineral composition. Journal of
891 African Earth Sciences, 49, 136–152.
892 Khalil, A. E. S., Obeid, M. A., and Azer, M.K. (2014) Serpentinized peridotites at the north part
893 of Wadi Allaqi district (Egypt): Implications for the tectono-magmatic evolution of fore-
894 arc crust. Acta Geologica Sinica, 88, Issue 5, 1421–1436.
895 Klemm, D. D., Klemm, R., and Murr, A. (2001) Gold of the Pharaohs — 6000 years of
896 goldmining in Egypt and Nubia. Journal of African Earth Sciences, 33, 643–659.

Koç, S., and Kadıoğlu, Y. K. (1996) Mineralogy, geochemistry and precious metal content of Karacakaya (Yunusemre-Eskisehir) listwaenites. Ofioliti, 21, 125-130.

Kranidiotis, P. and MacLean, W. H. (1987) The systematics of chlorite alteration at the Phelps Dodge massive sulfide deposit, Matagami, Quebec. Economic Geology, 82, 1898–1911.

Lebda, E. M. (1995) Petrology and Mineral Chemistry of Serpentinite Rocks of the Gogołow-Jordanow Massif, SW Poland. Ph.D. Thesis, Wrocław University, Poland, 189p.

Madu B. E., Nesbitt B. E., and Muehlenbachs K. (1990) A mesothermal gold-stibnite-quartz vein occurrence in the Canadian Cordillera. Economic Geology 85, 1260–1268.

McDonough, W. F. and Sun, S. S. (1995) Composition of the Earth: Chemical Geology 120, 223–253.

Meert, J. G. (2003) A synopsis of events related to the assembly of eastern Gondwana. Tectonophysics, 362, 1-40.

Mellini, M., Rumori, C., and Viti, C. (2005) Hydrothermally reset magmatic spinels in retrograde serpentinites: formation of 'ferritchromit' rims and chlorite aureoles. Contributions to Mineralogy and Petrology, 149, 266-275.

Mirnejad, H., Ebrahimi-Nasrabadi, K., Lalonde, A. E., and Taylor, B. E. (2008) Mineralogy, stable isotope geochemistry, and paragenesis of magnesite deposits from the ophiolite belt of Eastern Iran. Economic Geology, 103, 1703–1713.

Moghadam, H. S., Khedr, M. Z., Arai, S., Stern, R. J., Ghorbani, G., Tamura, A., and Ottley, C. J. (2015) Arc-related harzburgite–dunite–chromitite complexes in the mantle section of the Sabzevar ophiolite, Iran: a model for formation of podiform chromitites. Gondwana Research, 27, 575–593.

Newton, R. C. and Stern, R. J., 1990. A Late Precambrian CO_2 ''Event''. Geological Society of America Abstracts with Programs, Dallas, p. 190.

Oskierski H. C., Bailey J. G., Kennedy E. M., Jacobsen G., Ashley P. M. and Dlugogorski B. Z. (2013) Formation of weathering-derived magnesite deposits in the New England Orogen, New South Wales, Australia: implications from mineralogy, geochemistry and genesis of the Attunga magnesite deposit. Mineral Deposita 48, 525–541.

Obeid, M. A., Khalil, A. E. S., and Azer, M. K. (2016) Mineralogy, geochemistry and geotectonic significance of the Neoproterozoic ophiolite of Wadi Arais area, south Eastern Desert, Egypt. Internal Geological Review, 58, 687–702.

Ohara, Y., Stern, R. J., Ishii, T., Yurimoto, H., and Yamazaki, T. (2002) Peridotites from the Mariana Trough: first look at the mantle beneath an active back-arc basin. Contribution to Mineralogy and Petrology, 143, 1–18.

Osman, A. (1995) The mode of occurrence of gold-bearing listvenite at El Barramiya gold mine, Eastern desert, Egypt. Middle East Research Centre. Ain Shams University. Earth Sciences Series, 9, 93–103.

Oweiss, Kh. A., El Naggar, A. A., Abdel Razik, K. A., Moselhy, N., and Ali, A. B. (2001) Gold exploration at Heiani area, South Eastern Desert, Egypt. Annals Geological Survey of Egypt, XXIV, 435–450.

Page, P. and Barnes, S.J. (2009) Using trace elements in chromites to constrain the origin of podiform chromitites in the Thetford Mines Ophiolite, Québec, Canada. Economic Geology, 104, 997-1018.

Paulick, H., Bach, W., Godard, M., Hoog, C. J., Suhr, G., and Harvey, J. (2006) Geochemistry of abyssal peridotites (Mid-Atlantic Ridge, 15 20′N, ODP Leg 209): implications for fluid/rock interaction in slow spreading environments. Chemical Geology, 234, 179–210.

943 Pearce, J. A., Lippard, S. J., and Roberts, S. (1984) Characteristics and tectonic significance of
944 supra-subduction zone ophiolites. In: Kokelaar, P. B. and Howells, M. F. (eds) Marginal
945 basin geology. Geological Society of London, Special Publication, 16, 77–94.
946 Pearce, J. A., Barker, P. F., Edwards, S. J., Parkinson, I. J., and Leat, P. T. (2000) Geochemistry
947 and tectonic significance of peridotites from the South Sandwich arc-basin system, South
948 Atlantic. Contributions to Mineralogy and Petrology, 139, 36–53.
949 Proenza, J. A., Ortega-Gutierrez, F., Camprubi, A., Tritlla, J., Elias-Herrera, M., and Reyes-Salas,
950 M. (2004) Paleozoic serpentinites enclosed chromitites from Tehuitzingo (Acatlán
951 Complex, southern Mexico): a petrological and mineralogical study. Journal of South
952 American Earth Sciences, 16, 649–666.
953 Proenza, J. A., Zaccarini, F., Escayola, M., Cábana C., Shalamuk A., and Garuti G. (2008)
954 Composition and textures of chromite and platinum group minerals in chromitites of the
955 western ophiolitic belt from Pampean ranges of Córdoba, Argentina. Ore Geology
956 Reviews, 33(1), 32–48.
957 Qiu, T. and Zhua, Y. (2017) Chromian spinels in highly altered ultramafic rocks from the
958 Sartohay ophiolitic mélange, Xinjiang, NW China. Journal of Asian Earth Sciences
959 (https://doi.org/10.1016/j.jseaes.2017.08.011).
960 Ramadan, T. M. (2002) Exploration for gold-bearing listwaenites at Um Khasila area, Central
961 Eastern Desert, Egypt. Egyptian Journal of Remote Sensing and Space Sciences, 5, 63–
962 76.
963 Ramadan, T. M., Sadek, M. F., Abu El Leil, I., and Salem, S. M. (2005) Um El Touyur El Fuqani
964 gold mineralization, South Eastern Desert, Egypt: using Landsat ETM+ imagery. Annals
965 of Geological Survey of Egypt, 28, 263–281.

966 Rittmann, A. (1958) Geosynclinal volcanism, Ophiolites and Barramiya rocks. The Egyptian
967 Journal of Geology, 2, 61–66.
968 Robinson, P. T., Trumbull, R. B., Schmitt, A., Yang, J. S., Li, J. W., Zhou, M. F., and Xiong, F.
969 (2015) The origin and significance of crustal minerals in ophiolitic chromitites and
970 peridotites. Gondwana Research, 27, 486–506.
971 Saldi G. D., Schott J., Pokrovsky O. S., Gautier Q. and Oelkers E. H. (2012) An experimental
972 study of magnesite precipitation rates at neutral to alkaline conditions and 100–200 °C as
973 a function of pH, aqueous solution composition and chemical affinity. Geochimica et
974 Cosmochimica Acta, 83, 93-109.
975 Salem, I.A., Ghoneim, M. F., Zahran, A. A., and Hamdy, M. M. (1997) Petrology and genesis of
976 the ultramafic-hosted vein magnesite deposits at G. El-Rubshi, central Eastern Desert,
977 Egypt. 3rd International Conference on Geochemistry, Alexandria University, Alexandria-
978 Egypt, 241-267.
979 Salters, V. J. M. and Stracke, A. (2004) Composition of the depleted mantle. Geochemistry,
980 Geophysics, Geosystems, 5, Q05B07, 27p.
981 Saumur, B. M. and Hattori, K. (2013) Zoned Cr-spinel and ferritchromite alteration in forearc
982 mantle serpentinites of the Rio San Juan complex, Dominican Republic. Mineralogical
983 Magazine, 77, 117–136.
984 Schandl E. S. and Wicks F. J. (1993) Carbonate and associated alteration of ultramafic and
985 rhyolitic rocks at the Hemingway Property, Kidd Creek Volcanic Complex, Timmins,
986 Ontario. Economic Geology 88, 1615–1635.
987 Schandl E. S. and Gorton M. P. (2012) Hydrothermal alteration and CO_2 metasomatism (natural
988 carbon sequestration) of komatiites in the south-western Abitibi greenstone belt. Canadian
989 Mineralogist 50, 129–146.

990 Shackleton, R. M. (1994) Review of late Proterozoic sutures, ophiolitic mélanges and tectonics of
991 eastern Egypt and north Sudan. Geological Rundschau, 83, 537-546.
992 Shukri, N. M., and Lotfi, M. (1959) The Geology of the Bir Barramiya area. Bulletin of Faculty
993 of Science, Cairo University, 34, 83-130.
994 Singh, A. K., and Singh, R. B. (2013) Genetic implications of Zn- and Mn-rich Cr-spinels in
995 serpentinites of the Tidding Suture Zone, eastern Himalaya, NE India. Geological Journal,
996 48, 22–38.
997 Sobolev, N. V. and Logvinova, A. M. (2005) Significance of accessory chrome spinels in
998 identifying serpentinite paragenesis. International Geological Review 47, 58–64.
999 Sofiya, A., Ishiwatari, A., Hirano, N., and Tsujimori, T. (2017) Relict chromian spinels in Tulu
1000 Dimtu serpentinites and listvenite, Western Ethiopia: implications for the timing of
1001 listvenite formation. International Geology Review, 59, 1621-1631.
1002 Spiridonov E. M. (1991) Listvenites and zodites. International Geology Review 33, 397–407.
1003
1004 Stern, R. J. (1994) Arc assembly and continental collision in the Neoproterozoic East African
1005 Orogen: implications for the consolidation of Gondwanaland. Annual Reviews of Earth
1006 and Planetary Science, 22, 319-351.
1007 Stern, R. J. (2002) Crustal evolution in the East African Orogen: a neodymium isotopic
1008 perspective. Journal of African Earth Sciences, 34,109–117.
1009 Stern, R. J., and Hedge, C. E. (1985) Geochronologic constraints on late Precambrian crustal
1010 evolution in the Eastern Desert of Egypt. American Journal of Science, 285, 319–351.
1011 Stern, R. J., and Gwinn, C. J. (1990) Origin of Late Precambrian Intrusive Carbonates, Eastern
1012 Desert of Egypt and Sudan: C, O, and Sr Isotopic Evidence. Precambrian Research, 46,
1013 259–272.

1014 Stern, R. J., Johnson, P. R., Kröner, A., and Yibas, B. (2004) Neoproterozoic ophiolites of the
1015 Arabian-Nubian Shield. In: Kusky, T. M. (ed.), Precambrian Ophiolites and Related
1016 Rocks. In: Developments in Precambrian Geology, Amsterdam, Elsevier, 13, 95–128.
1017 Stoeser, D. B. and Frost, C. D. (2006) Nd, Pb, Sr and O isotopic characterization of Saudi
1018 Arabian Shield terranes. Chemical Geology, 226, 163–188.
1019 Takahashi, E., Uto, K., and Schilling, J. G. (1987) Primary magma compositions and Mg/Fe
1020 ratios of their mantle residues along mid-Atlantic ridge 29N to 73N Technical Report, A9.
1021 Institute of Studies Earth's Interior, Okayama University Series, pp.1–14.
1022 Uçurum, A. (2000) Listwaenites in Turkey: Perspectives on formation and precious metal
1023 concentration with reference to occurrences in East-Central Anatolia. Ofioliti, 25, 15-29.
1024 Uçurum, A. and Larson, L.T. (1999) Geology, base precious metal concentration and genesis of
1025 the silica-carbonate alteration (listwaenites) from Late Cretaceous ophiolitic mélanges at
1026 Cürek-Divriği in Sivas province and at Güvenç, Karakuz Hekimhan in Malatya province,
1027 Central East Turkey. Chemie der Erde Geochemistry, 59, 77-104.
1028 Uysal, I., Yalçin Ersoy, E., Karsli, O., Dilek, Y., Burhan Sadiklar, M., Ottley, C. J., Tiepolo, M.,
1029 and Meisel, T. (2012) Coexistence of abyssal and ultra-depleted SSZ type mantle
1030 peridotites in a Neo-Tethyan Ophiolite in SW Turkey: Constraints from mineral
1031 composition, whole-rock geochemistry (major-trace-REE-PGE), and Re-Os isotope
1032 systematics. Lithos, 132-133, 50-69.
1033 Weir R. H. and Kerrick D. M. (1987) Mineralogic, fluid inclusion, and stable isotope studies of
1034 several gold-mines in the Mother Lode, Tuolumne and Mariposa Counties, California.
1035 Economic Geology 82, 328–344.
1036 Wilde A., Simpson L. and Hanna S. (2002) Preliminary study of Cenozoic alteration and
1037 platinum deposition in the Oman ophiolite. J. Virtual Explorer 6, 7–13.

Yavuz, F., Kumral, M., Karakaya, N., Karakaya, M. C., and Yildirim, D. K. (2015) A Windows program for chlorite calculation and classification. Computers and Geosciences, 81, 101–113.

Zedef, V., Russell, M. J., Fallick, A. E., and Hall, A. J. (2000) Genesis of vein stockwork and sedimentary magnesite and hydromagnesite deposits in the ultramafic terrains of southwestern Turkey: a stable isotope study. Economic Geology, 95, 429–446.

Zhou, M. F., Robinson, P. T., Malpas, J., and Zijin, L. (1996) Podiform chromite in the Luobusa ophiolite (Southern Tibet): implication for melt rock interaction and chromite segregation in the upper mantle. Journal of Petrology, 37, 3–21.

Zimmer, M., Kröner, A., Jochum, K. P., Reischmann, T., and Todt, W. (1995) The Gabal Gerf complex: a Precambrian N-MORB ophiolite in the Nubian Shield, NE Africa. Chemical Geology, 123, 29-51.

Zoheir, B. (2011) Transpressional zones in ophiolitic mélange terranes: Potential exploration targets for gold in the South Eastern Desert, Egypt. Journal of Geochemical Exploration, 111, 23–38.

Zoheir, B. A. and Lehmann, B. (2011) Listvenite-lode association at the Barramiya gold mine, Eastern Desert, Egypt. Ore Geology Reviews, 39, 101-115.

Zoheir, B. and Moritz, R. (2014) Fluid evolution in the El-Sid gold deposit, Eastern Desert, Egypt, in Garofalo, P. S., and Ridley, J. R., eds., Gold-transporting hydrothermal fluids in the Earth's crust. London, Geological Society, Special Publications, 402 p.

Captions of Figures

Figure 1. Distribution of ophiolitic rocks in the Eastern Desert of Egypt (modified after Shackleton 1994); the location of the study region (Fig. 2) is indicated.

Figure 2. Geologic map of Gabal Sirsir area, modified after Zoheir (2011).

Figure 3. (a) Field photo showing sheared serpentinite and listwaenite (type-I), (b) Hand specimen of sheared listwaenite (type-I) with oriented quartz and carbonates. (c) Field photo showing massive listwaenite (type-II), and d) Hand specimen of massive listwaenite (type-II) with quartz veins.

Figure 4. Photomicrographs showing petrographic textures under crossed nicols (a, b, c, d and f) and reflected light (e, g and h). Abbreviations: Ol=olivine, Cb=carbonates, Spl=spinel, Fu=Fuschite, Srp=serpentine, Qtz=quartz, Mt=magnetite. (a) Fresh relic of olivine within serpentinite; (b) Bastite texture after orthopyroxene; (c) antigorite crystals intergrown with magnesite; (d) Scattered blocky aggregates of carbonates within serpentinite; (e) Large chromian spinel crystal with pristine core followed by an irregular light-grey ferritchromite zone and a grey-white magnetite rim; (f) fuchsite flakes with a perfect cleavage in one direction; (g) chromian spinel in listwaenite overprinted by thin rims of ferritchromite along margins and later cracks; and (h) chromian spinel in Type II listwaenite-like rock highly altered to ferritchromite.

Figure 5. (a) Mg# vs. NiO (wt%) of olivine from G. Sirsir serpentinized peridotites. The mantle olivine array is adopted from Takahashi et al. (1987); the field of olivine in Egyptian ophiolites is drawn based on the published data of Khalil and Azer (2007), Khalil et al. (2014), Gahlan et al. (2015) and Obeid et al. (2016); and the field of Egyptian layered intrusions is based on published data of Ghoneim (1989), Helmy and El-Mahallawi (2003), Farahat and Helmy (2006), Azer and El-Gharbawy (2011), Helmy and Mahallawi (2003), Abd El- Rahman et al. (2012), and Azer et al. (2016, 2017). (b) Cr–Al– Fe^{3+} plot

for chromian spinel and its alteration products in the serpentinized peridotites and listwaenite. (c) Cr# versus Mg# of chromian spinel cores in serpentinite and Type I listwaenite (adopted from Stern et al. 2004). MORB = mid-ocean ridge basalt. (d) Cr_2O_3 versus Al_2O_3 of fuchsite in Type I listwaenite.

Figure 6. Cr# of spinel vs. Fo content of coexisting olivine from serpentinized peridotites (Arai 1992, 1994). PM: primitive mantle; OSMA: olivine-spinel mantle array. The degree of melt extraction is based on spinel composition (after Hellebrand et al. 2001 and Uysal et al. 2012).

Table 1. Major and trace elements of serpentinites and listwaenitic rocks of G. Sirsir area, south Eastern Desert, Egypt.

Rock type	Serpentinites									Listwaenitic rocks						
										Type I listwaenite						
Sample No.	SR2	SR12	SR15	SR22	SR31	SR37	SR40	SR44	SR49	SR5	SR7	SR10	SR17	SR20	SR23	SR26
Major oxides in wt.%																
SiO_2	40.41	39.86	36.97	37.06	38.47	37.82	38.39	38.05	37.81	38.89	41.36	40.28	39.72	42.02	46.17	47.57
TiO_2	0.05	0.04	<0.02	0.03	0.03	0.03	0.02	<0.02	0.04	0.19	0.17	0.24	0.2	0.15	0.06	0.08
Al_2O_3	0.54	0.29	0.51	1.01	0.41	0.65	0.78	0.28	0.54	1.23	1.99	1.52	2.06	1.71	1.22	1.16
$Fe_2O_3^T$	6.88	6.56	7.62	7.21	7.08	5.96	7.57	6.09	7.13	8.28	8.36	9.09	8.17	7.96	6.43	6.04
MnO	0.07	0.07	0.07	0.05	0.12	0.08	0.12	0.09	0.07	0.07	0.13	0.08	0.11	0.13	0.08	0.11
MgO	39.06	38.83	39.22	40.13	38.26	39.86	38.42	39.34	39.13	24.38	22.24	21.53	22.11	20.58	20.84	21.3
CaO	0.03	0.31	0.04	0.83	0.05	0.09	0.65	0.07	0.15	6.89	5.34	7.06	6.61	7.05	12.58	10.23
Na_2O	0.01	0.04	0.02	0.01	<0.01	<0.01	0.01	<0.01	0.01	0.41	0.96	0.62	1.27	0.86	0.13	0.25
K_2O	0.02	0.01	<0.01	0.02	<0.01	<0.01	0.02	<0.01	0.01	1.21	1.24	1.87	2.51	1.66	0.11	0.13
P_2O_5	<0.01	<0.01	0.01	0.03	<0.01	<0.01	<0.01	0.02	0.02	0.09	0.08	0.06	0.07	0.11	0.04	0.02
LOI	12.55	13.44	14.94	13.3	14.84	15.06	13.34	15.43	14.83	17.89	18.09	17.11	16.89	17.51	11.46	12.48
Total	99.62	99.45	99.4	99.68	99.26	99.55	99.32	99.37	99.74	99.53	99.96	99.46	99.72	99.74	99.12	99.37
Mg#	91.0	91.3	90.2	90.8	90.6	92.3	90.0	92.0	90.7	84.0	82.6	80.9	82.8	82.2	85.2	86.3
Trace elements in ppm																
Sc	6.5	5.8	7.6	6.1	7.7	8.3	3.2	2.6	6.1	4.2	10.2	13.5	7.8	11.3	3.7	4.4
V	32.4	26.1	31.8	32.7	27.5	33.4	41.2	b.d.l.	35	47	39	50	47	36	30	38
Cr	2436	1789	2814	2237	2090	2562	1802	1519	2088	2249	2147	2316	2471	2765	987	1256
Co	96.4	117.2	102.6	105.2	120.3	100.1	118.2	104.6	98	69	58	51	62	78	29	28
Ni	2058	1718	1984	2005	2132	2134	1921	2274	1931	1764	1979	1244	1837	2021	897	1051
Rb	0.2	<0.1	0.1	<0.1	0.5	0.3	0.2	<0.1	0.2	2.3	1.7	4.8	2.5	3.6	1.9	1.2
Sr	2	3	5	3	7	0.9	1	4	0.6	112	127	164	142	169	110	123
Y	0.1	<0.1	<0.1	0.2	0.2	<0.1	<0.1	0.1	0.1	0.8	1.6	0.5	1.1	1.5	0.8	1.4
Nb	<0.1	<0.1	<0.1	0.1	0.1	<0.1	<0.1	0.1	<0.1	0.1	<0.1	0.2	<0.1	0.2	0.3	0.4
Cs	<0.1	0.2	<0.1	0.3	<0.1	0.1	<0.1	0.1	0.2	<0.1	0.1	<0.1	0.2	0.1	0.4	<0.1
Pb	0.2	0.1	0.2	0.3	0.5	0.4	0.5	0.2	0.2	4	3	2	1	3	11	6
Ta	0.1	<0.1	<0.1	0.2	<0.1	0.2	<0.1	0.1	<0.1	0.1	<0.1	0.1	<0.1	0.2	0.2	<0.1
Ba	4	7	6	5	5	6	4	3	2	72	94	108	137	114	32	21
Th	<0.2	<0.2	<0.2	0.3	0.2	<0.2	<0.2	<0.2	0.1	<0.2	0.2	<0.2	0.3	<0.2	0.2	<0.2
U	<0.1	<0.1	0.1	0.3	<0.1	<0.1	0.1	<0.1	0.2	0.2	0.4	0.2	<0.1	0.3	0.2	0.5
Au (ppb)	10.7	6.5	4.7	6.3	8.1	5.8	4.1	5.8	5.7	1446	573	871	1157	2008	2011	4987
Sb	1.7	0.9	0.8	1.2	1.4	1.3	0.8	0.7	1.1	0.7	1.9	4.3	6.8	7.5	1.41	2.8
As	9.4	8.9	6.2	7.3	5.6	7.8	8.2	6.7	7.4	156	183	211	256	282	223	197
Cu	53	28	33	40	47	53	31	24	35	32	78	44	56	73	114	95
Ag	<0.1	0.1	0.2	0.2	<0.1	0.1	0.2	<0.1	0.2	0.3	0.4	0.5	0.6	0.3	0.9	0.7
Zn	39	33	28	32	31	29	41	35	36	65	113	58	107	105	80	113

Type II listwaenite				
SR28	SR31	SR34	SR46	SR52
48.48	56.21	49.36	47.76	45.68
0.28	1.14	0.14	0.09	0.06
0.93	0.68	0.92	0.74	0.86
5.04	4.03	5.73	6.63	6.34
0.17	0.08	0.07	0.06	0.13
17.92	13.44	19.99	21.31	21.72
12.65	10.19	8.81	8.94	9.93
0.08	0.11	0.09	0.15	0.14
0.22	0.56	0.21	0.19	0.12
0.03	0.05	0.01	0.02	0.03
13.27	14.11	14.78	13.62	14.45
99.07	100.6	100.11	99.51	99.46
86.4	85.6	86.1	85.1	85.9
5.1	3.2	6.9	4.5	3.3
41	34	45	29	33
598	1026	815	752	867
32	42	58	63	37
1121	956	1214	965	941
3.7	5.6	3.4	1.8	1.7
134	128	102	137	164
1.1	0.5	0.7	1.3	0.4
0.4	<0.1	0.2	<0.1	0.3
0.1	<0.1	<0.1	0.3	0.2
5	8	4	7	5
0.1	0.2	<0.1	0.1	0.3
35	27	18	22	29
0.2	<0.2	0.3	0.4	<0.2
0.4	0.7	0.3	0.4	0.6
2231	1854	1502	6584	1871
5.6	6.9	8.8	8.7	9.2
301	326	254	207	186
82	109	77	100	93
1.1	1	0.8	1.7	1.4
44	87	103	64	57

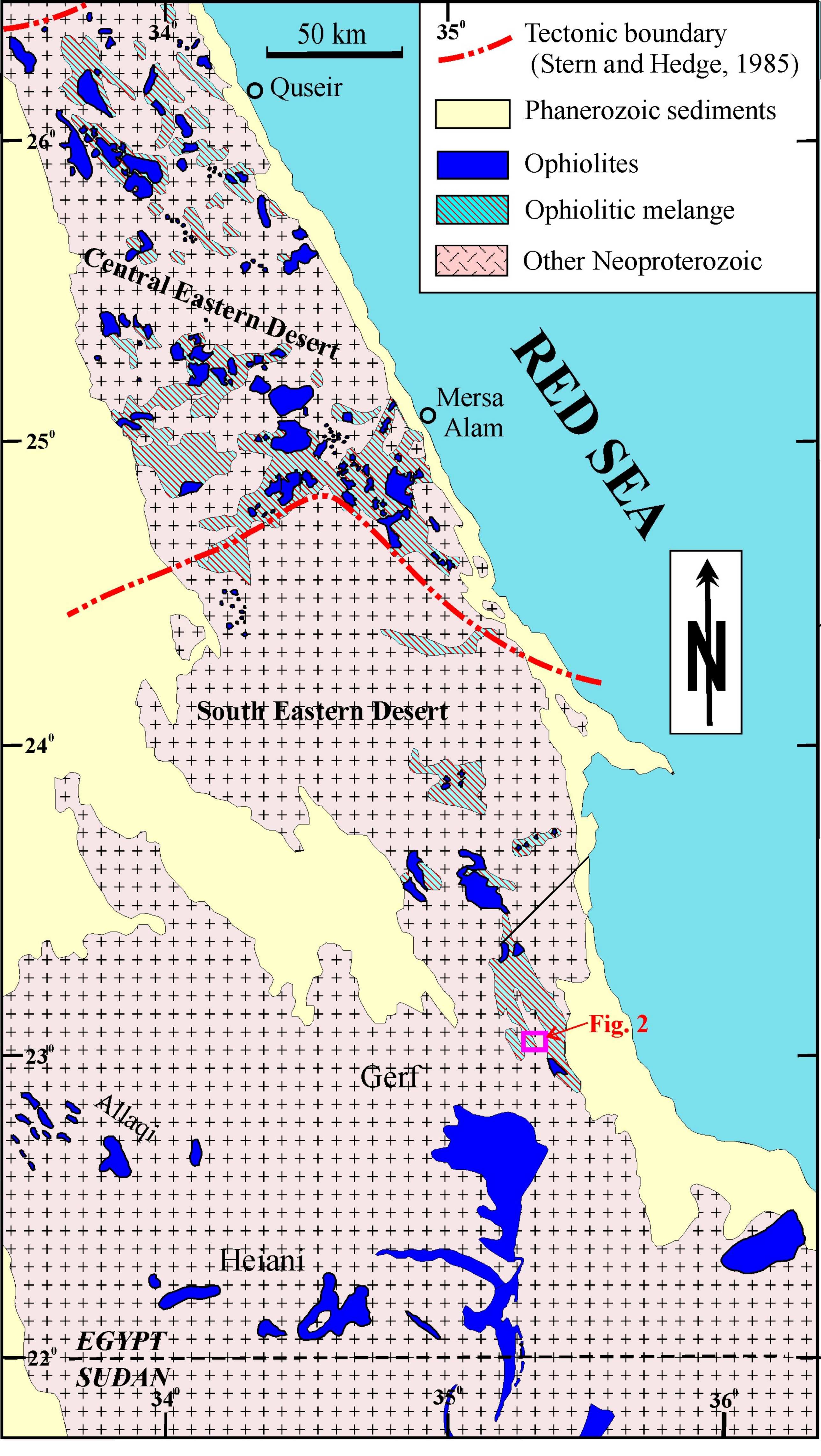
50 km
Quseir
Mersa Alam
RED SEA
Central Eastern Desert
South Eastern Desert
Gerf
Allaqi
Heiani
EGYPT
SUDAN
Fig. 2
N
Tectonic boundary (Stern and Hedge, 1985)
Phanerozoic sediments
Ophiolites
Ophiolitic melange
Other Neoproterozoic
34°
35°
36°
22°
23°
24°
25°
26°

Figure 1

35°|18′ 35°|20′ 35°|22

23°|10′ 23°|08′ 23°|06′

G. Sirsir

Wadi Hodein

G. El-Anbat

0 1 2 km

LEGEND

- Sample location
- Anticline
- Strike and dip
- Fault plane
- Thrust Fault
- Wadi deposits
- Late/post -orogenic granite
- Syn-orogenic granite
- Metarhyolitic rocks
- Metaandesitic rocks
- Ophiolitic melange
- Listwaenite
- Pillow metabasalt
- Metagabbro
- Serpentinites


a
Serpentinite
Listwaenite

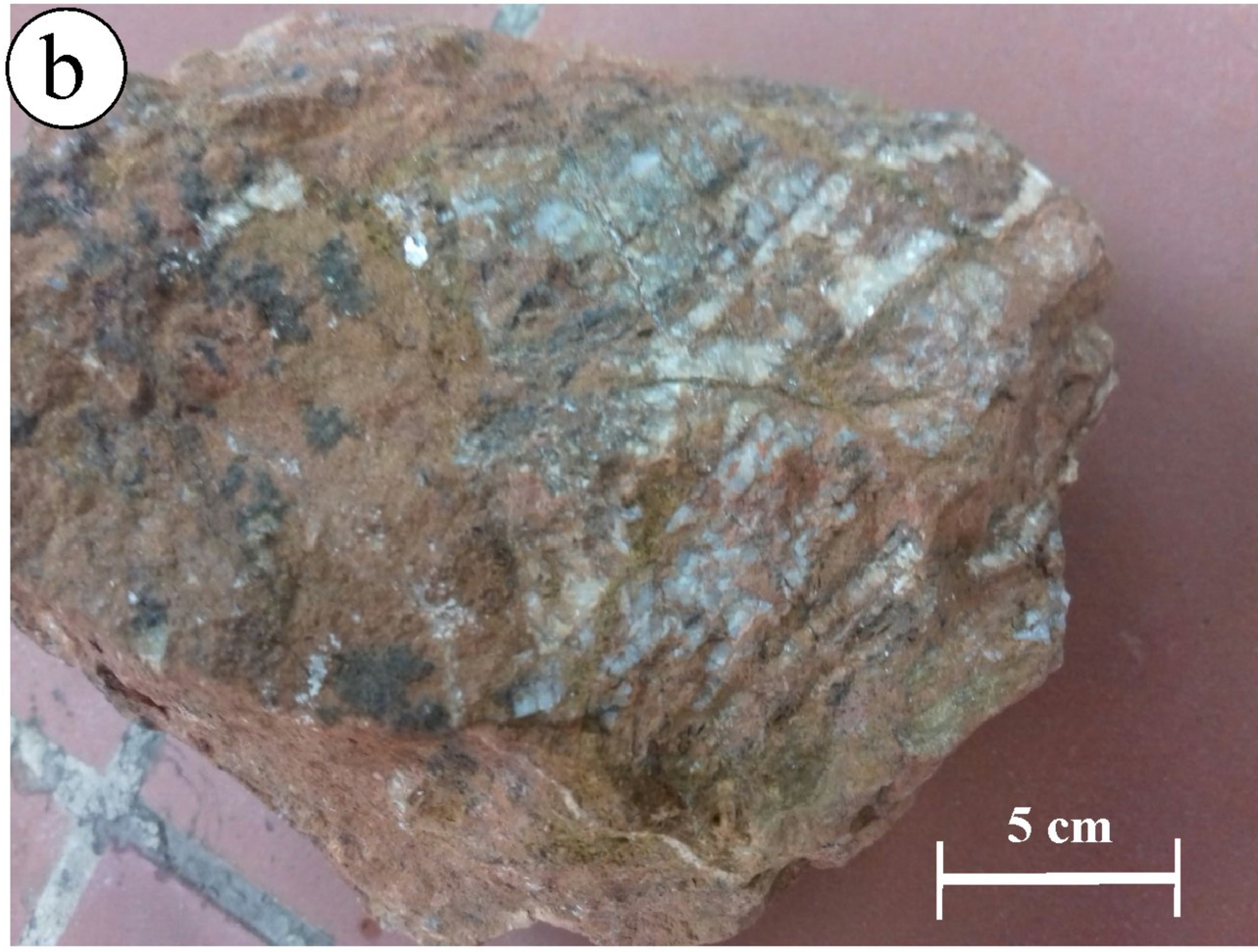
b
5 cm


c
Serpentinite
Listwaenite


d
5 cm

Figure 3

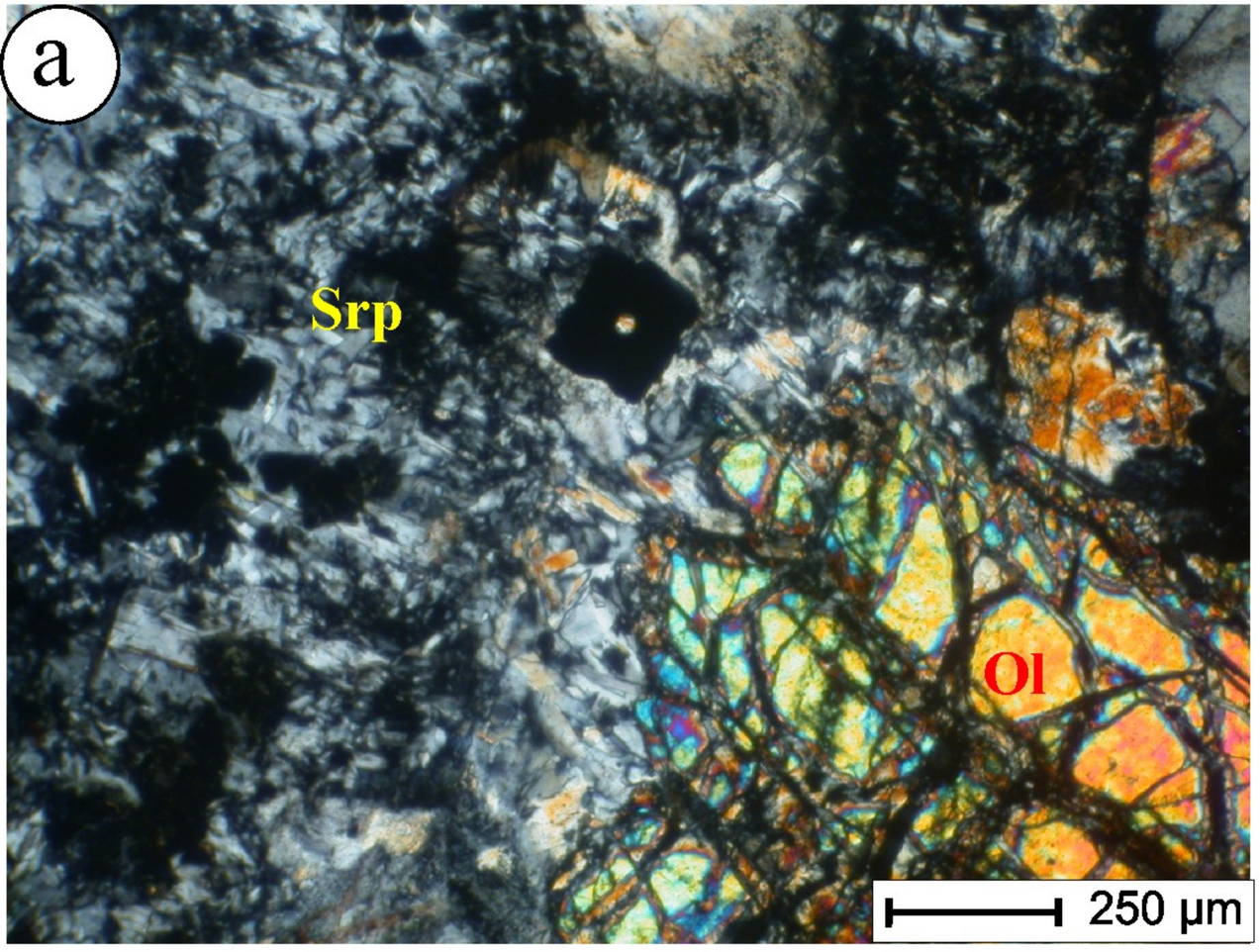
a
Srp
Ol
250 µm

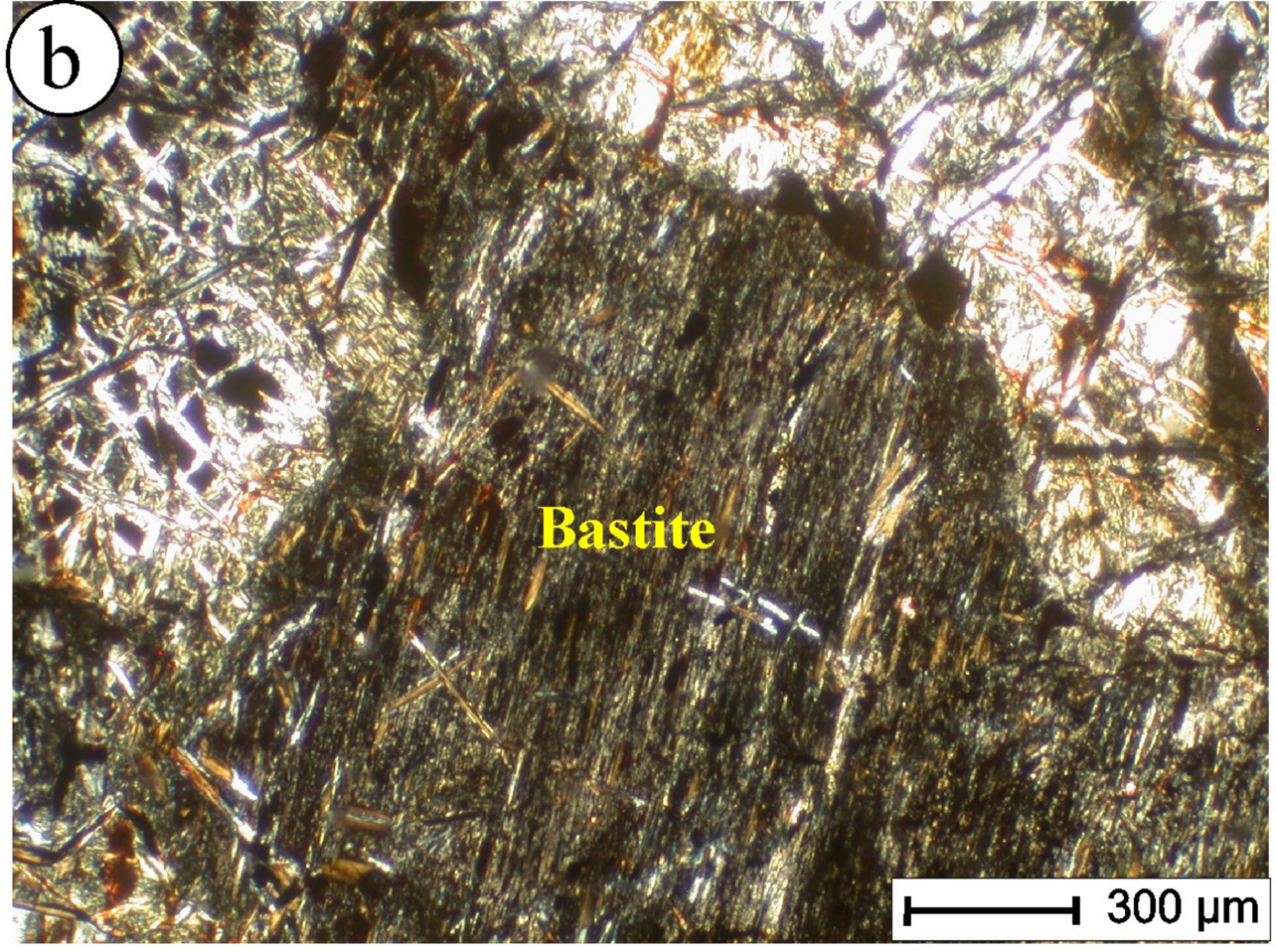
b
Bastite
300 µm

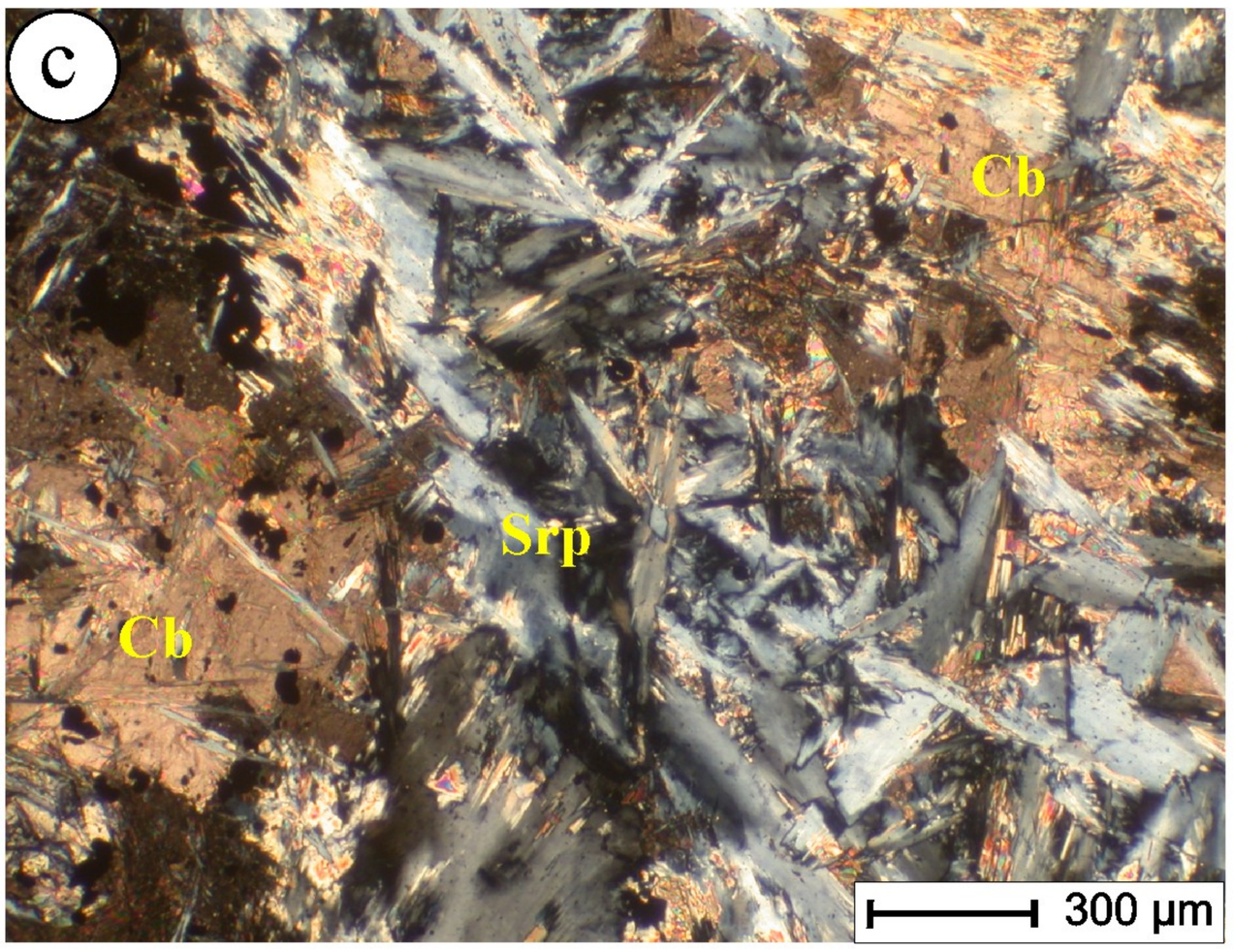
c
Cb
Srp
Cb
300 µm

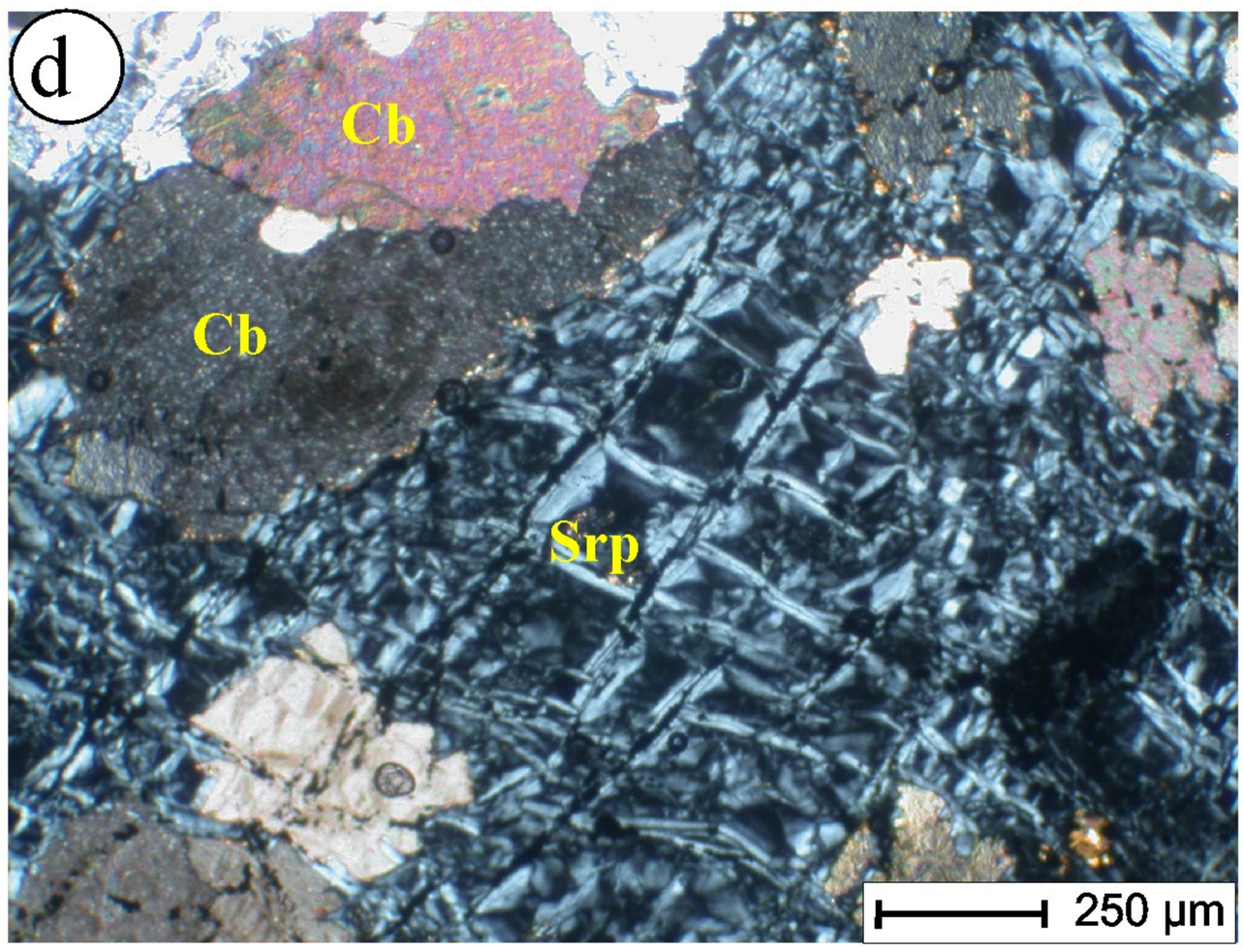
d
Cb
Cb
Srp
250 µm

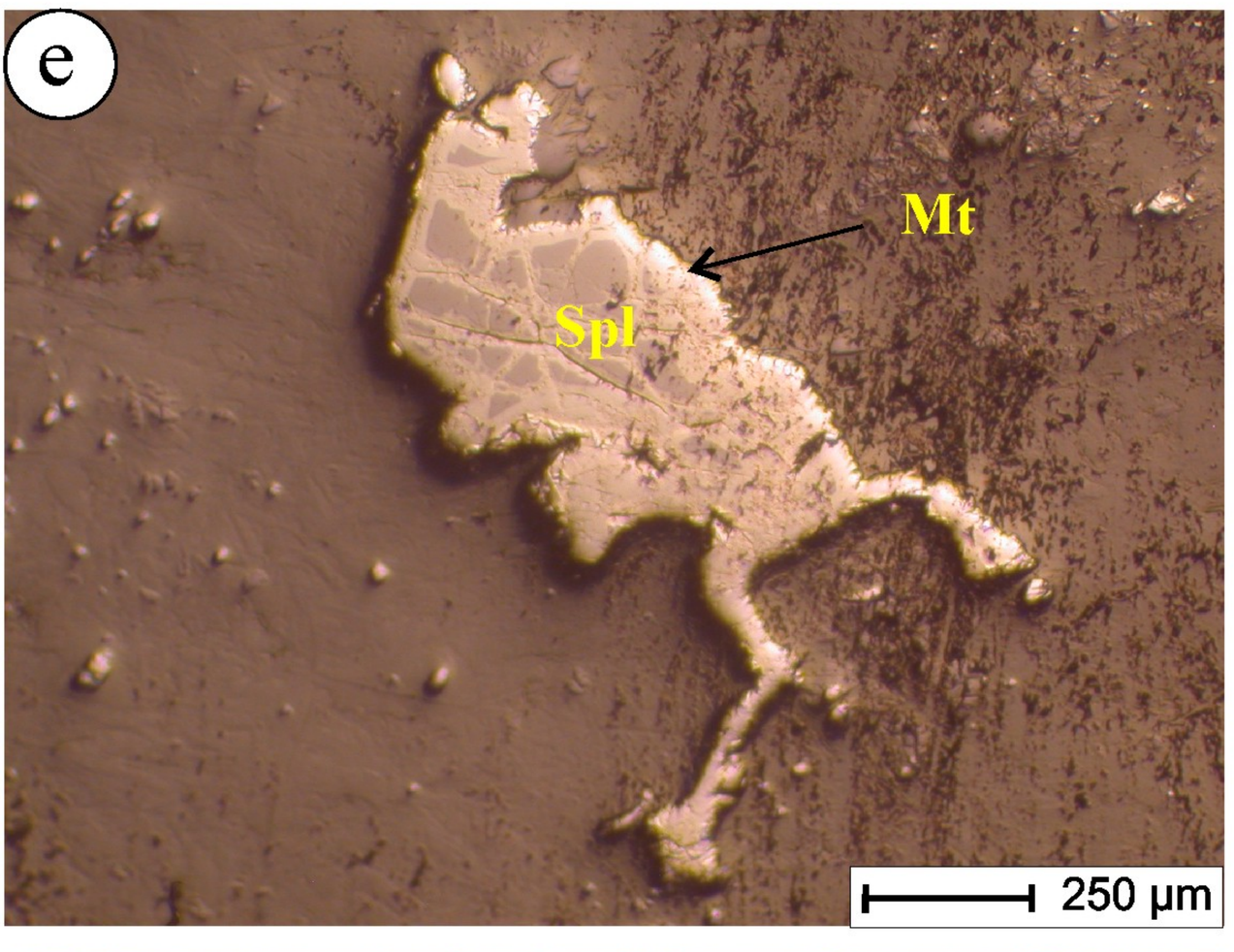
e
Mt
Spl
250 µm

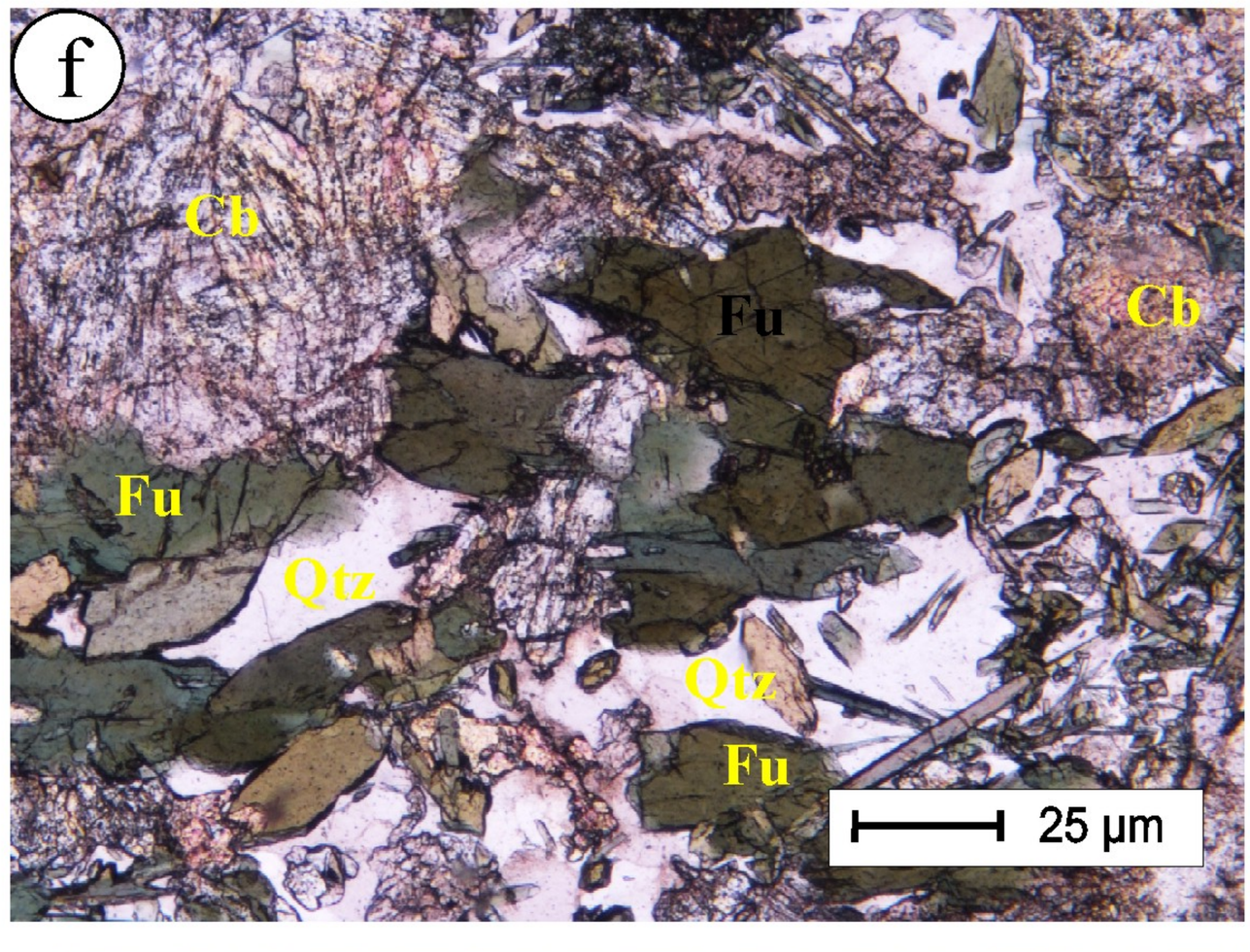
f
Cb
Fu
Cb
Fu
Qtz
Qtz
Fu
25 µm

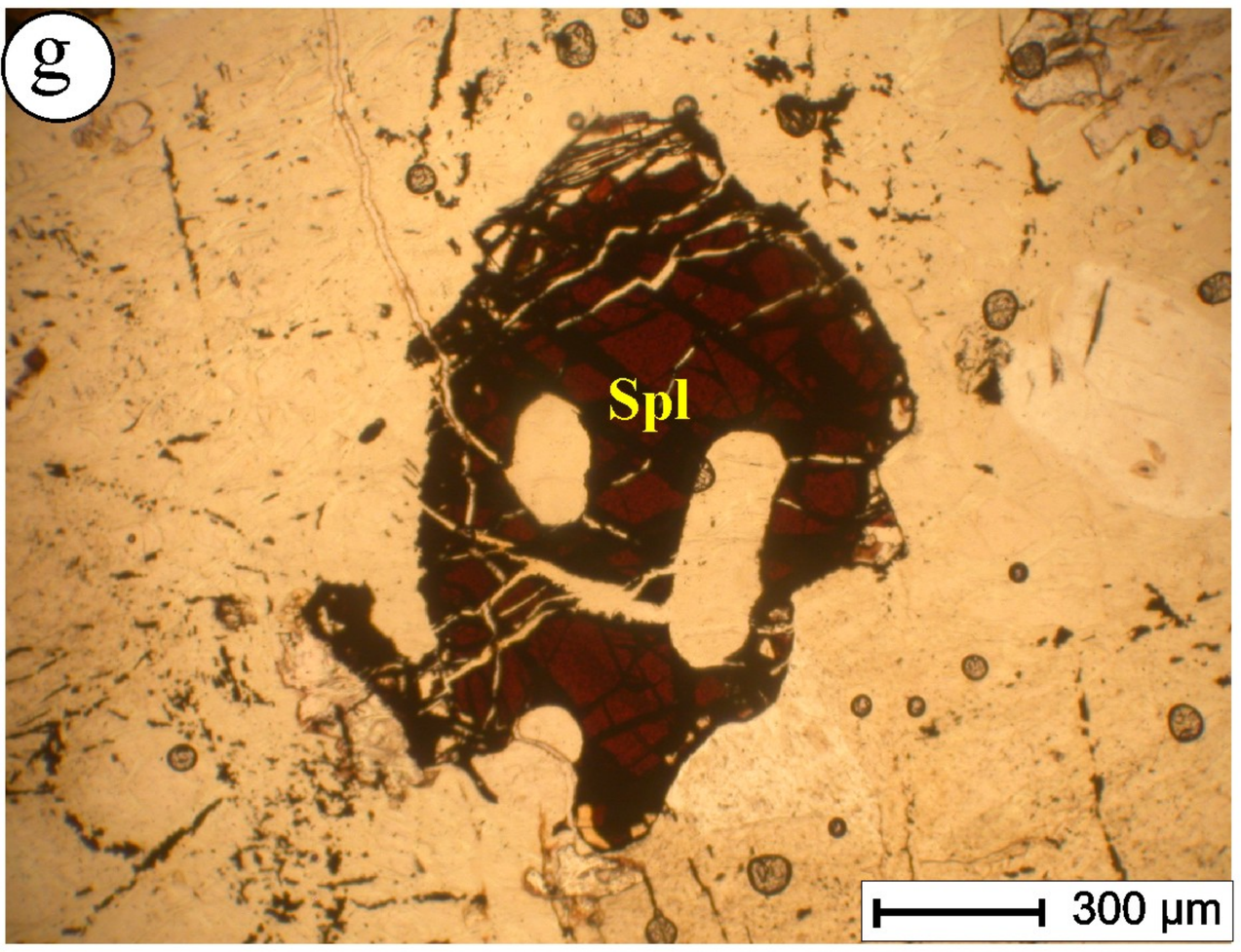
g
Spl
300 µm

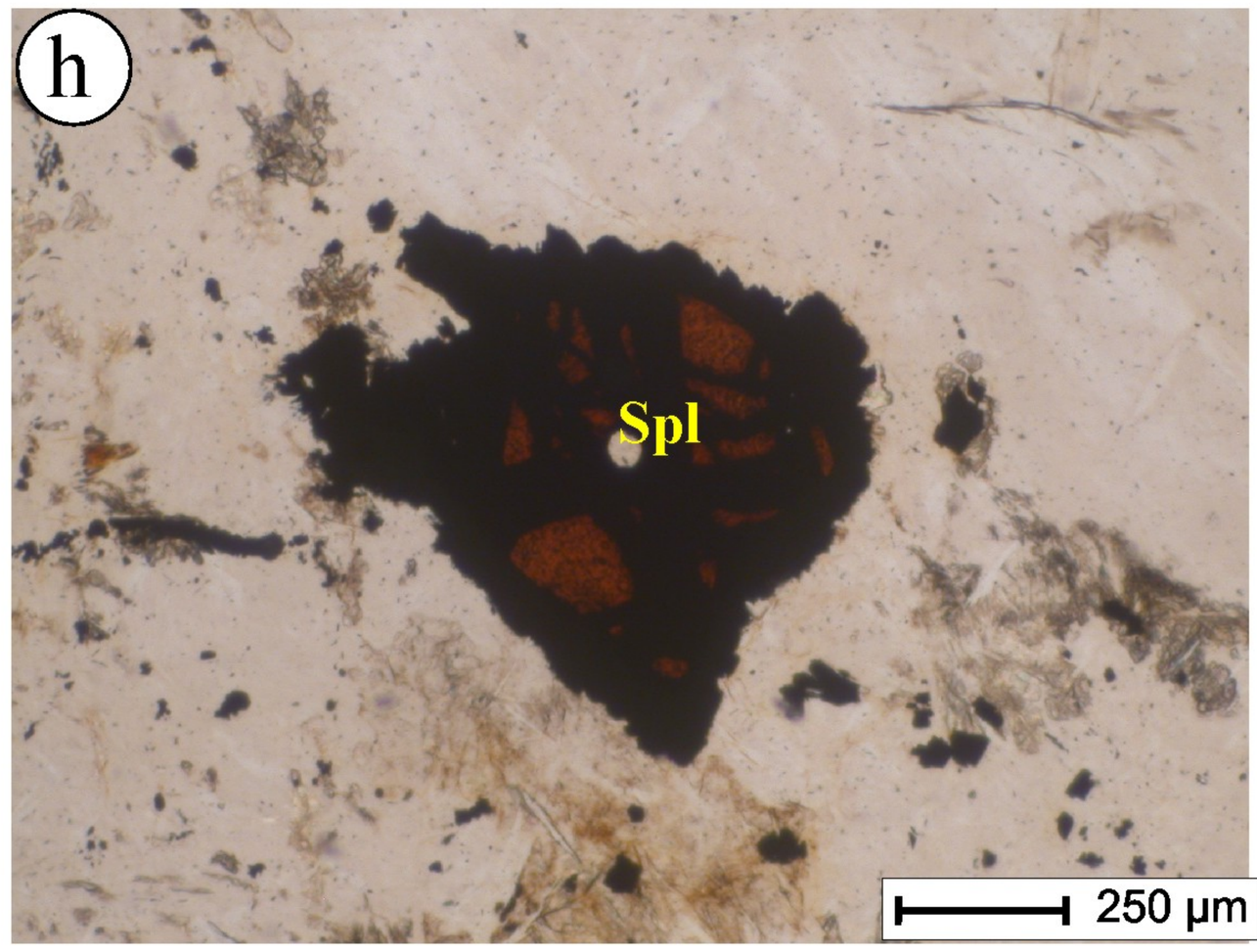
h
Spl
250 µm

Figure 4

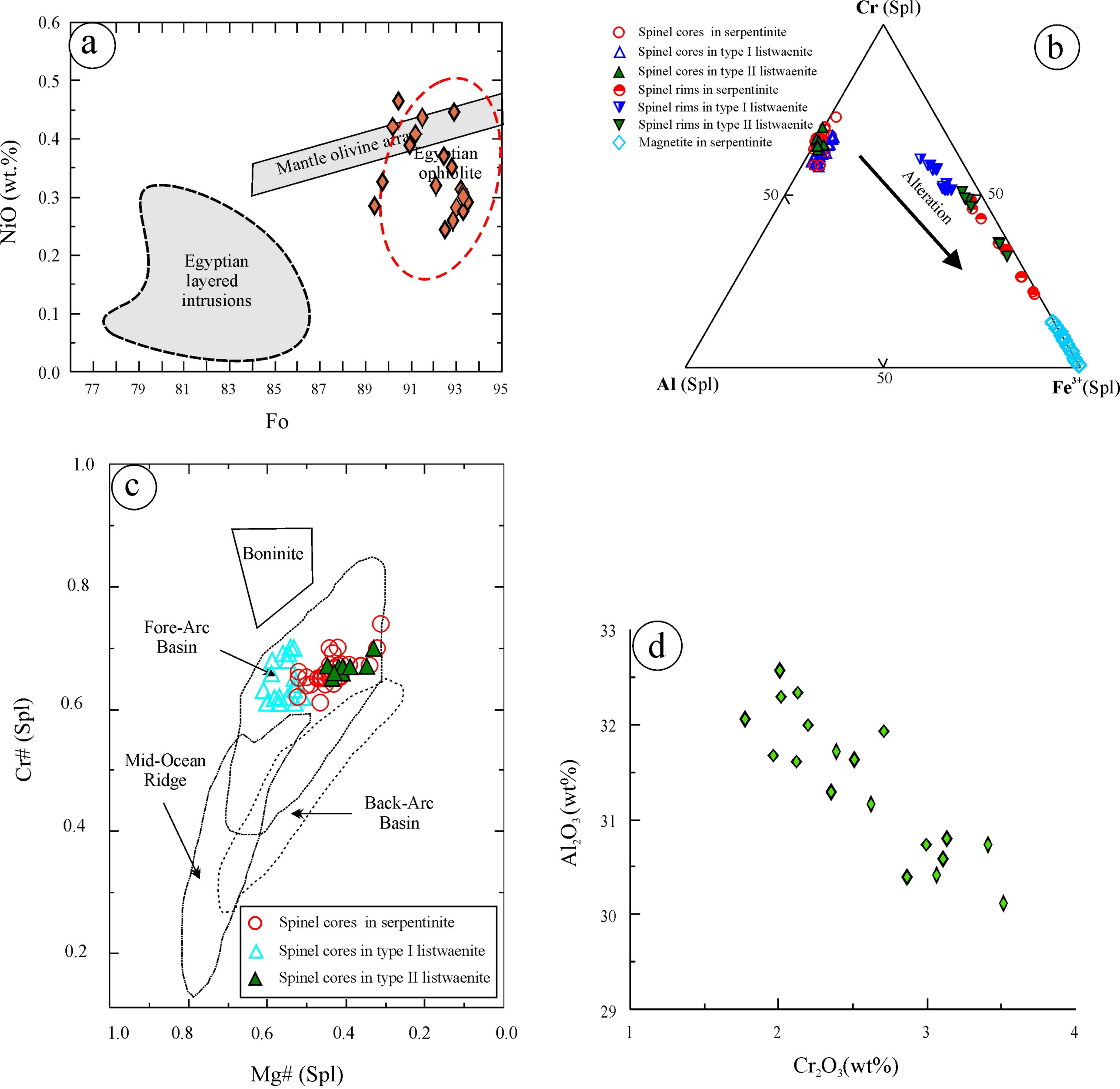
a
NiO (wt.%)
Fo
Mantle olivine array
Egyptian ophiolite
Egyptian layered intrusions
b
Cr (Spl)
Al (Spl)
Fe3+(Spl)
Spinel cores in serpentinite
Spinel cores in type I listwaenite
Spinel cores in type II listwaenite
Spinel rims in serpentinite
Spinel rims in type I listwaenite
Spinel rims in type II listwaenite
Magnetite in serpentinite
Alteration
50
c
Cr# (Spl)
Mg# (Spl)
Boninite
Fore-Arc Basin
Mid-Ocean Ridge
Back-Arc Basin
d
Al2O3 (wt%)
Cr2O3(wt%)

Figure 5

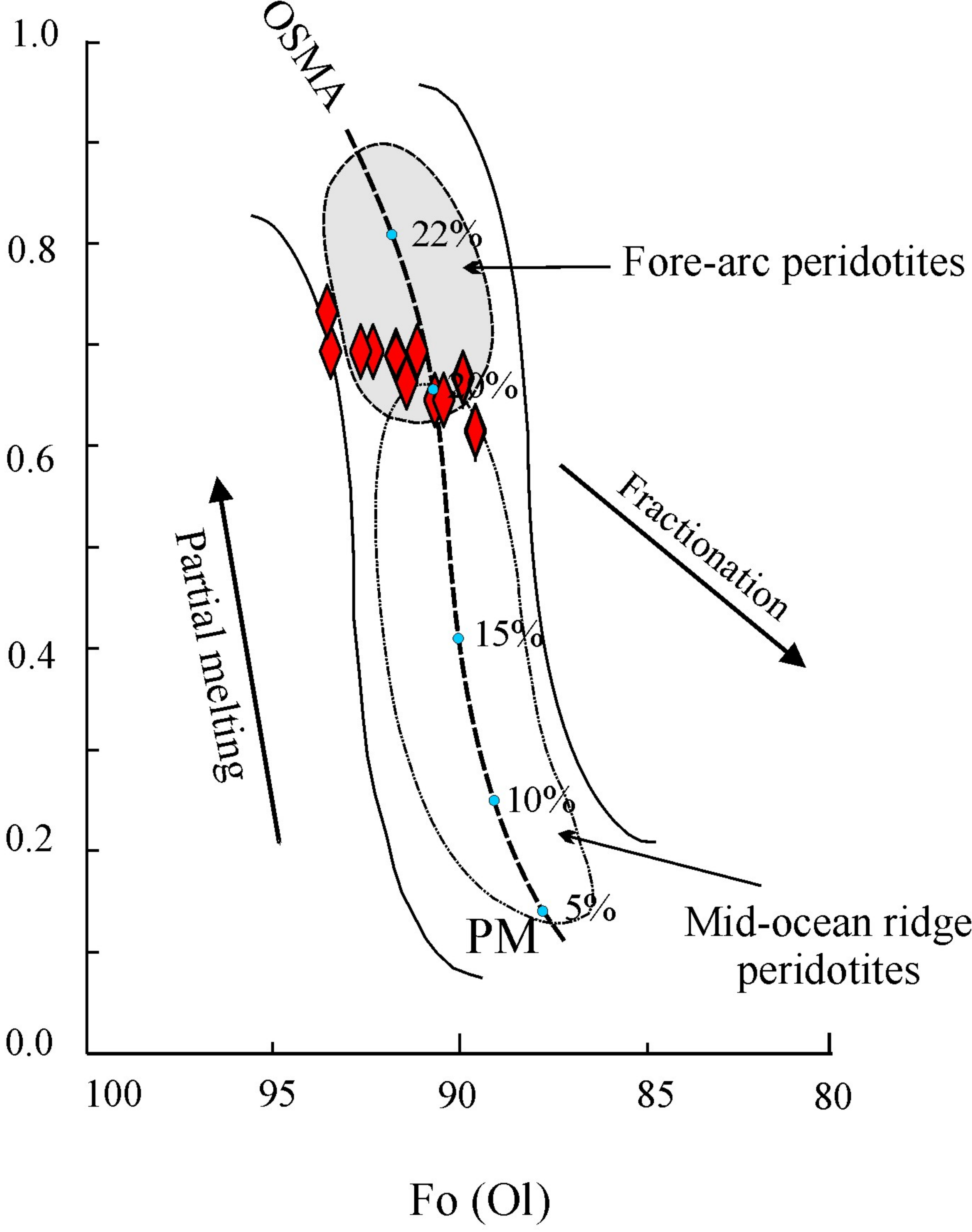
OSMA
22%
Fore-arc peridotites
Fractionation
Partial melting
15%
10%
5%
PM
Mid-ocean ridge
peridotites
1.0
0.8
0.6
0.4
0.2
0.0
Cr# (Spl)
100
95
90
85
80
Fo (Ol)

Figure 6